DESIGN AND OPTIMIZATION OF EFFICIENT MICROFLUIDIC PLATFORMS FOR PARTICLE MANIPULATION AND CELL STIMULATION IN SYSTEMS BIOLOGY

A Dissertation
Presented to
The Academic Faculty

by

Alison Marie Paul

In Partial Fulfillment
of the Requirements for the Degree
Doctor of Philosophy in the
School of School of Chemical and Biomolecular Engineering

Georgia Institute of Technology
December 2011

DESIGN AND OPTIMIZATION OF EFFICIENT MICROFLUIDIC PLATFORMS FOR PARTICLE MANIPULATION AND CELL STIMULATION IN SYSTEMS BIOLOGY

Approved by:

Dr. Hang Lu, Advisor
School of Chemical and Biomolecular Engineering
Georgia Institute of Technology

Dr. Melissa Kemp
School of Biomedical Engineering
Georgia Institute of Technology

Dr. Victor Breedveld
School of Chemical and Biomolecular Engineering
Georgia Institute of Technology

Dr. William Koros
School of Chemical and Biomolecular Engineering
Georgia Institute of Technology

Dr. Andres Garcia
School of Mechanical Engineering
Georgia Institute of Technology

Date Approved: July 27, 2011

ACKNOWLEDGEMENTS

This work could not have been accomplished without the guidance and support from many people. First, I thank my advisor, Professor Hang Lu, for her guidance over the years here. She always saw the best in every situation and pushed me to be the best I could be. Her support in allowing me to pursue my new passion for teaching while continuing my dissertation work was above and beyond that expected of her and I am grateful. Also, I thank my committee members Professor Victor Breedveld, Professor Andres Garcia, Professor Melissa Kemp, and Professor William Koros who provided valuable insight and guidance. I specifically thank Melissa Kemp for her collaboration and allowing me to sit in on her journal club meetings to better understand what it means to study cell signaling networks.

I thank all the member of the Lu Research Group for allowing me to talk through my research problems and for their helpful ideas, company and camaraderie. Specifically, I thank Jeffery Stirman for his technical assistance across the board. The breadth of his knowledge never ceases to impress me. Also, I thank Matt Crane and Ivan Cáceres for answering my endless MATLAB questions. I appreciate Edward Park and Kwanghun Chung for leading the way and developing a solid base for our research group. Additionally, I thank Catherine Rivet for being the best collaborator and co-author.

During my tenure I had the privilege to work with 2 amazing undergraduate students. I thank Boyang (Michael) Zhang for all is hard work at the beginning of the particle mixing work. He was willing to try anything and asked many intelligent

questions that eventually lead us to the development of the STEP imaging technique. Also, I thank Nicholas Harris for his endless hours in the lab and interesting conversation about research (and some marathon running).

I thank all of my teaching mentors in CETL and CEISMC especially Donna Llewellyn and Marion Usselman. Also, I thank Professor Pradeep Agrawal for amazing mentorship during my teaching practicum.

I am grateful to all my Chemical Engineering classmates for great friendship though out the years especially Andria Deaguero, Josh Hutcheson, Richard Moore, and Eric Ping. Finally and most importantly, I thank my Mom, Dad, Stepfather, sister Alexandra, and brother Daniel for their constant prayers and support.

TABLE OF CONTENTS

LIST OF TABLES

LIST OF FIGURES

SUMMARY

The overall goal of this research is to develop an efficient microfluidic system to study signal transduction in stimulation dynamics. This research applied reactive transport fundamentals in concert with biological systems knowledge to completely understand diffusion of soluble signals, fluid and particle flow properties, and dynamics of cellular responses.

First, a device capable of parallel multi-time-point cell stimulation and lysis on-chip was developed in collaboration with Catherine Rivet and Melissa Kemp. This two-module microfluidic platform for simultaneous multi-time point stimulation and lysis of T Cells for early time point signaling activation has resolution down to 20 seconds using only small amounts of cells and reagents. The key design features were rapid mixing of reagents and uniform splitting into 8 channels for simultaneous collection of multi-time point data. Chaotic mixing was investigated via computational fluid dynamic modeling, and was used to achieve rapid and complete mixing. This modular device is flexible - with easy adjustment of the setup, a wide range of time points can be achieved. Treatment in the device did not elicit adverse cellular stress in Jurkat cells. Activation of 6 important proteins in the signaling cascade was quantified upon stimulation with a soluble form of α-CD3. The dynamics from device and conventional methods were similar, but the micro device exhibited significantly less error between experiments.

Second, manipulation of cells (and particles) in complex flow environments is important to the microfluidic device design. This requires knowing how they interact with and behave in fluids in three dimensions. Current methods, such as confocal

microscopy, for visualizing flow in 3D are expensive or limited to extremely small particles in slow flows. To understand flow of cells through complex 3-D flow schemes, a Single-field Three-dimensional Epifluorescence Particle (STEP) imaging technique was developed. This technique uses epifluorescent images of moving particles taken at a single focal plane and the pattern of out of focus light to determine the particles' distance from the focal plane based on empirical correlations. It is easy to use, requires only a conventional epifluorescence microscope, and yet provides single particle information faster and with potentially more spatial information than confocal microscopy. Using the STEP imaging technique, we were able to determine particle distributions and track individual particles in complex flow geometries.

Finally, during the design of the stimulation device it was observed that the cells do not distribute across the channel in the same way as the fluids. While solute mixing was fast and efficient, the cells were not evenly distributed across 8 time point channels. For efficient device operation a better mixer design was needed for cells. To that end, the effects of Reynolds number, channel geometry and particle size on mixing were evaluated using the STEP imaging technique. The particle distributions under a variety of experimental conditions were analyzed and mixing efficiency was evaluated by calculating Shannon entropy. Based on the observation that geometry and particle size were most influential factors on particle distribution, it was hypothesized that our earlier observation and all observed phenomena in the range of our experiments were due to the inability of particles of finite size to access all streamlines of the complex flow geometry. To test this hypothesis, a computational model was generated to track particles through

the complex flow geometries and determine the best geometry for mixing cells. The model captured the major features of the experimental particle distributions.

Overall, this work contributed to the realization of microfluidic platforms as powerful tools for probing areas of biology and medicine that are difficult with existing technology. This high-throughput format enabled simple and fast generation of large sets of quantitative data, with consistent sample handling. The particle distribution experiments and model were the necessary first steps to designing efficient unit operations (specifically mixing, separation, and sample concentration) on cells in microfluidic devices. The model can be used for informed design of unit operations in many applications in the future.

CHAPTER 1

INTRODUCTION

1.1 Cell signaling dynamics

Understanding the dynamics of cell signaling networks is central to many biological applications, especially in complex disease phenotypes related to cancer, immune responses, development, and potential pharmacological interferences. In the natural environment, cells encounter a variety of signals that regulate their behavior. These signals include soluble growth factors and cytokines and can be complex, varying both space and time. Signals are mainly sensed by transmembrane receptors and transduced by complex biochemical pathways to control cell growth, movement, and functionality. Pathways involved in cell maintenance and apoptosis are studied extensively to understand cancer development [1, 2]. To date, focus on particular signal-transduction cascades and molecules has provided system-level insights into mechanism-based drug discovery [3, 4].

Immune-based therapies are increasingly being recognized as powerful tools in the fight against cancer. Adoptive transfer therapy aims to harness the power of the adaptive immune response for fighting tumors as "foreign" bodies. Groundbreaking studies of adoptive transfer for treating metastatic melanoma [5, 6] resulted in a number of pursuits in clinical trials against metastatic melanoma and many other types of cancers [7]. Many of the existing clinical trials utilize autologous T cells that are refined for their specificity or engineered to enhance their activity [8].

Despite adoptive transfer therapy's initial success, practical hurdles remain before it becomes a viable clinical option for cancer treatment. The largest hurdle lies in the sheer number of cells needed for transfusion, typically 10^9-10^{11} cells per patient. Therefore, *ex vivo* expansion is necessary. Many such techniques have recently emerged for expanding T cells *in vitro* [9-13]. For the success of this treatment, tumor antigen-specific T cells must maintain uniform responsiveness and specificity after *ex vivo* expansion and once in the tumor environment. Uniformity and standardization of the T cell expansion process are required for reproducibility and clinical translation [9]. To insure success of adoptive transfer therapy, T cell clones need to be evaluated before transfer, based upon their specificity or functionality, regardless of diverse in vivo priming, selection or expansion method. Similarly, the evaluation of T cell clones in elderly population can enable the identification of immune risk profiles correlated with increased risk of immune dysfunction and increased mortality by generating an "immune signature" [14].

Multivariate analysis is a powerful tool to shed light on biological mechanisms and predicting cellular responses [10, 15]. Methods for evaluating T cell functionality will be useful not only for evaluation of the expansion quality, but can offer insight into changes of cellular function during expansion. Unraveling the mechanisms for functional alteration will not only provide insight into possible failure mechanisms in the expansion process, but would be helpful in determining how tumor cells inhibit T cell activity.

Intracellular immunostaining techniques via flow cytometry have proven useful for studying signaling pathways [13]; however the multi-laser cytometers are constrained for the number of proteins monitored. Cell lysis and biochemical detection of population

averages remains the most widespread method of capturing intracellular signaling dynamics of protein pathways. To extract the necessary protein information the cell must be stimulated for a precise period of time and immediately lysed to extract intracellular proteins for downstream analysis. A major challenge in signaling research is that many of these important protein activation events, such as phosphorylation, occur within minutes after stimulation [12, 16, 17]. Prior proteomic studies indicate widespread phosphorylation of signaling molecules occur within 5 minutes of T-Cell activation [18].

1.2 The limitations of conventional methods

Building a system-level computational model and gaining insights in to the complex signaling networks requires large data sets, presently a bottleneck in the process. For example, gene expression patterns or protein activity at various time points during stimulation with an external signal must be known; it usually takes labs years to accumulate a large body of this type of data [11, 19, 20]. Quantitative data not only at precise time points but early in the cells' response are necessary for accurate model generation. With conventional multi-well plate assays it is difficult to achieve adequate resolution at sub-minute timescales.

Additionally, current methods of analysis generate mostly qualitative and low content data. While sophisticated algorithms for systems level modeling now exist, the large data sets needed to completely understand how cells integrate all the information presented are less than adequate. Therefore, data generation is rate-limiting in systems biology model development.

1.3 Promise of microfluidic technology

Central to improving the speed and accuracy of data generation is the development of new high-throughput techniques. Microfluidic technology has emerged over the last few decades as a viable platform for well controlled experimental conditions with the ability to manipulate fluids precisely and efficiently. Several salient features make microfluidic devices ideal for this application: microfluidic systems are inexpensive and require relatively small sample volumes for experiments, conserving valuable cells and reagents; fluid behavior is predictable, allowing precise fluid manipulation and control; and parallel processing of samples is possible, increasing the amount of data available from one experiment [21, 22]. Additionally, precisely controlling the cellular microenvironment, microfluidics is capable of providing uniformity in sample handling to reduce error between experiments. Applications of microdevices in cell biology and analysis systems include cell cultivation, cell manipulation, cell separation and sorting, drug discovery and screening, and cell signaling. To date, many microdevices have already been developed for successfully culturing cells, stimulating with soluble factors, assaying gene expression and performing lysis [23-32].

El-Ali *et al.* developed a device achieving cell stimulus and lysis on a microfluidic chip using segmented gas-liquid flow for rapid mixing [26]. This device was the first to demonstrate on-chip multiple step manipulation of cells with fast mixing, thereby allowing access to the early time-point detection of protein states. However, this device did not allow for parallel experimentation. A separate experiment for each time point was necessary. Because multiple time points are needed to gather information on dynamics, the creation of a device capable of multiple time point stimulations

simultaneously would greatly decrease the time cost for generating the large amounts of data necessary.

The challenges of any on-chip assays are that the devices should minimize stress on the cells, should provide reproducible results from experiment to experiment, should produce quantitative results comparable to or better than bench-top schemes, should be scalable to high throughput format, should minimize consumption of cells and reagents, and ideally provide the temporal resolution that the bench-top counterparts cannot achieve. So far no chip-based designs have achieved all these criteria simultaneously.

1.4 Unit operations on cells in microfluidic technology

Microfluidic devices have become widely used for chemical and biological applications [21, 33], in many instances involving mixing and separation [34]. Both solutes (e.g. macromolecules and salts) and particulates (e.g. cells) are routinely mixed, separated, assayed, and processed using microfluidics [35-38], with the benefit of finer spatiotemporal control over traditional macro scale techniques. Continuous manipulation of cells and particles is important to many applications in biology and medicine [21, 39-41]. In particular, mixing of cells with reagents is an important step in many biological experiments [21, 26, 36]. For our application in Chapter 2, multi-time point stimulation of T-cells, complete lateral mixing is necessary for efficient cell distribution across the 8 outlets.

The staggered herringbone mixer (SHM) is an effective mixer for solutes (and bringing solutes to suspended cells) because in this device the two fluids are subjected to a sequence of rotational and extensional local flows that decrease characteristic length for

diffusion [37, 42]. However, we observed that for neutrally buoyant cells of finite size the distribution is dissimilar to that of the solutes and not uniform after long mixing time. This behavior was deterministic and highly reproducible. Understanding how cells and particles flow through complex flow geometries and the variables that govern their flow is necessary for design of efficient unit operations in multiphase microfluidic systems, including mixing and separation for many applications.

The effects of inertia, density, deformability and volume fraction on particle distributions are well characterized in many microfluidic systems [43-48]. DiCarlo et al demonstrated the lateral focusing of particles due to the existence of inertial forces in microfluidic channels [44]. This phenomenon originally observed in centimeter-scale systems by Segre and Silberberg [49]. Inertial lift forces focus randomly distributed particles continuously and at high rates to in 4 distinct regions in a square channel. This, however, cannot explain the behavior observed in the SHM mixer. This phenomenon only occurs at particle Reynolds numbers approaching 1 and above. Our experiments were performed at a maximum particle Reynolds number of 0.01 so the inertial lift does not completely explain our observations.

Hsu et al. showed these herringbone style mixers to align particles at different positions in the channel based on their density difference from the fluid. Particles more dense than the fluid focus at one position and those less dense at another [48]. Our experiments were performed in a density matched medium (using 7% dextran) to prevent cell settling, so this also does not explain our observations.

Howard Stone has shown extensively that deformability of red blood cells strongly influences the cell distribution in confined microfluidic channels [46]. To rule

this out, we compared the distribution of rigid beads to that of beads of the same size. The distribution of rigid beads was consistent with that of the cells, ruling out deformability as a main cause of our observed behavior.

Finally shear induced particle migration causes ~2 μm particles to segregate to form areas of high particle concentration in SHMs at high particle volume fractions, above 0.1 [47]. In our experiment, however, the maximum volume fraction used was 0.001. Again, this does not explain our observations.

1.5 Particle imaging in three dimensions

Having three-dimensional spatial information is a necessary step towards designing the next generation mixers, separators and manipulators and improving their performances as particles may behave differently when flows are rotated, split, and combined. Currently available techniques include confocal [50] and epifluorescent microscopy [51-60]. Although confocal microscopy can directly acquire 3D information, it is expensive, and more importantly, it does not provide information about individual particles due to the discretized nature of image acquisition. Some examples of epifluorescent approaches use additional cameras [51] or integrated micro mirrors [52] to acquire images from more than one angle, and then extract particle positions from those images. These approaches require additional equipment and are challenging to integrate with most microfluidic systems. Finally, many particle image velocimetry (PIV) applications measure the shape and spread of the particles' diffraction patterns to resolve their distance from the focal plane [53-60].

While these techniques are successful and in some cases very precise, they are limited to relatively slow flows and sub-micron particles that are assumed to follow the streamlines (to obtain information of fluid flow). In existing MicroPIV techniques the sub-micron particles can be approximates as a point source and the diffraction pattern can be predicted using optics theory [61]. In many applications, however, larger particles do not necessarily follow streamlines [62, 63]. This regime is of interest to many biological applications in mixing and separation of cells. For larger particles, the observed diffraction pattern is convoluted. There is no direct way to calculate the intensity pattern. Therefore, an empirical correlation is needed.

1.6 Thesis objectives

The purpose of this thesis is to design a lab-on-a-chip platform, for multiple time-point lymphocyte stimulation and lysis for downstream analysis of protein activation. The main research objective is to design a microfluidic device for cellular stimulation that will 1) minimize stress on the cells, 2) provide reproducible results from experiment to experiment, 3) produce quantitative results comparable to or better than bench-top schemes, 4) be scalable to high throughput formats, 5) minimize consumption of cells and reagents, and 6) provide the temporal resolution that the bench-top counterparts cannot achieve. Rapid mixing techniques and resistive splitting of reagents into each time-point channel were used for precise definition of multiple stimulation times. Proper execution of the main objective requires, complete mixing of the cell with stimulus and lysis buffer. To accomplish this, we developed an imaging technique to characterization of the cell mixing behavior in complex flow geometries.

1.7 Thesis outline

This thesis is divided into five chapters. Chapter two discusses the design and characterization of the microfluidic device for cell stimulation. Then Chapter three presents a novel our novel imaging techniques used to characterize the flow of cells and particles in complex flow systems. Chapter four discusses the cell and particle distributions in complex flow geometries. Finally, chapter five presents an overall discussion to this dissertation, concluding remarks and suggestions for future work to improve the efficiency and utility of the microsystem.

CHAPTER 2[†]

A MICROFLUIDIC PLATFORM FOR PARALLEL, MULIT-TIME POINT T CELL STIMULATION

2.1Overview

This chapter presents a lab-on-a-chip platform for multiple time-point lymphocyte stimulation and lysis for downstream analysis of protein activation adapted from Reference [36]. Mixing and even splitting of reagents into each time-point channel are key features of the design.

To understand over time how multiple proteins in the signaling network behave upon stimulation, vastly different incubation periods are required. Therefore we have designed our device for 8 time points in parallel with controlled rapid mixing, precisely timed stimulation, and rapid lysis. In addition, in this work we also circumvent the large shear at the gas-liquid interface in the earlier work. We show that our assay platform does not induce stress responses to the cells and yields reproducible and quantitative protein activity information with small numbers of cells.

This work uses the emerging microfluidic technology to increase the throughput and accuracy of this data generation. This technology takes advantage of the uniformity and controllability in sample handling and treatment to reduce error associated with biochemical assays with a minimal requirement of cells in a high- throughput and parallel fashion [36, 64].

[†] Adapted from Hirsch, A.M., et al., *Parallel multi-time point cell stimulation and lysis on-chip for studying early signaling events in T cell activation.* Lab on a Chip, 2009. **9**(4): p. 536 - 544.

2.2 Experimental design

In order to achieve precise incubation control on multiple time scales, we took a two-module approach for increased system flexibility (Figure 2-1). In our design, pressure-driven flow (by syringe pumps) entered at only 3 inlets -- cells, stimulus and lysis buffer -- which made handling multiple samples and parallel experiments simple. Cells and stimulus were mixed and split into 8 equal streams in less than 0.25 seconds on Module 1. The majority of the incubation time (~20 seconds to 5 minutes in our experiments) occurred in the tubing leading to Module 2. On Module 2 the reaction was quenched and cells were lysed by mixing with cold lysis buffer, in less than 1 second, to extract intracellular components. Mixing and balancing flow-rates were important to the design, which we describe below.

2.2.1 Rapid mixing to ensure precise stimulation times

For precise definition of stimulation time, especially for the very early time points (e.g. 20 seconds), rapid mixing of cells with reagents was essential to our design. Mixing is necessary in multiple steps of the assay: the cells first have to be mixed with the stimulant, and then once incubated for the desired duration they have to be mixed again with lysis buffer to yield lysate for downstream biochemical assays. If mixing takes a significant portion of the time compared to stimulation and lysis incubation, cells suspended in the initial medium will be introduced to the stimulant at different times, and the contact time cannot be precisely controlled. This non-uniformity of contact time would make it difficult to define and repeat the "stimulation time".

We considered a few existing designs of microfluidic mixers. El-Ali *et al* have shown a gas/liquid segmented flow scheme to enhance mixing [26]. The advantage of

this mixing scheme is that it is very fast and the throughput is high; however, because the mixing scheme relies on the circulation of the liquid behind gas bubbles, the shear is large at the multiphase interface and can introduce undesired lysis and/or mechanotransduction in cells. Ugaz *et al.*[65] demonstrated Dean flow mixing, which is simple and could be suitable for many biological experiments since it is gentle. However, for Dean flow mixers, better mixing correlates to higher Reynolds' numbers ($\mathrm{Re} = \rho \cdot v \cdot L / \mu$ where ρ is the density of the fluid, μ the viscosity, v the linear velocity, and L the channel's limiting dimension, is a measure of the inertial effect over viscous effect of fluid flow). To implement this mixing scheme for our application would require large flow rates that render the subsequent incubation step impractical. We chose the asymmetric herringbone mixer (SHM) [66]. The mixing time in these devices are sufficiently short for our application and the shear is minimal. There is no analytical solution to the mixing scheme, and a limited number of experiments have been performed on such mixer designs [42, 67, 68]. Optimized parameters, asymmetry of the herringbones (2/3 of the way across the channel) and angle with respect to y-axis (45^{o}), from Stroock *et al.* were used as a starting point in this design[66].

In order to design proper mixers for our application and determine an accurate starting time of incubation, we developed computational fluid dynamics (CFD) models for different geometries and experimental flow conditions using COMSOL (Stockholm, Sweden), a finite element solver for non-linear partial differential equations. Because our buffers, cell solutions, and stimulation solutions can have different fluidic properties, the model was also used to probe the mixing effects of viscosity and density. Furthermore

confocal microscopy experiments were used to visualize the mixing of solutions with mismatched viscosity.

2.2.2 Flow splitting and precisely-controlled stimulation

After mixing, the fluid was split into 8 streams on Module 1. Each stream accomplished a different time point in the tubing leading to Module 2. For efficient device operation, it was necessary for equal volumes of sample to be collected for each time point. Equal flow rates in each stream were achieved by balancing the channel resistance. The resistance, proportional to fluidic pressure drop and a function of channel dimensions, increases with increasing length and decreasing cross-sectional area. From the Hagen-Poiseulle equation,

$$\Delta P = \frac{128\mu \cdot Q \cdot L}{\pi \cdot d^4} \qquad (1)$$

where ΔP is pressure drop, μ is viscosity, Q is volumetric flow rate, L is path length, and d is the diameter, we calculated a relationship for resistance (R) based on channel dimensions.

$$R \propto \frac{L}{d^4} \qquad (2)$$

Since the microfluidic channels are square, when implementing these equations a hydrodynamic diameter was used,

$$d = \frac{2(h \cdot w)}{h + w} \quad (3)$$

where h is the channel height and w is the channel width. This hydrodynamic diameter definition neglects the effect of channel shape, but suits our application in determining order of magnitude resistance differences between tubing and channels. All the lengths

and widths of the microfluidic channels are the same in each time point channel to achieve equal resistance.

The stimulation time is defined by residence time in the device. This time is the sum of the residence time in the channels and the residence time in the tubing leading to the lysis module (Module 2).

$$t = \frac{L_c h_c w_c}{Q} + \frac{L_t \pi \cdot ID_t}{Q} \qquad (4)$$

The subscripts *c* and *t* denote channels and tubing, respectively, and *ID* is the inner diameter.

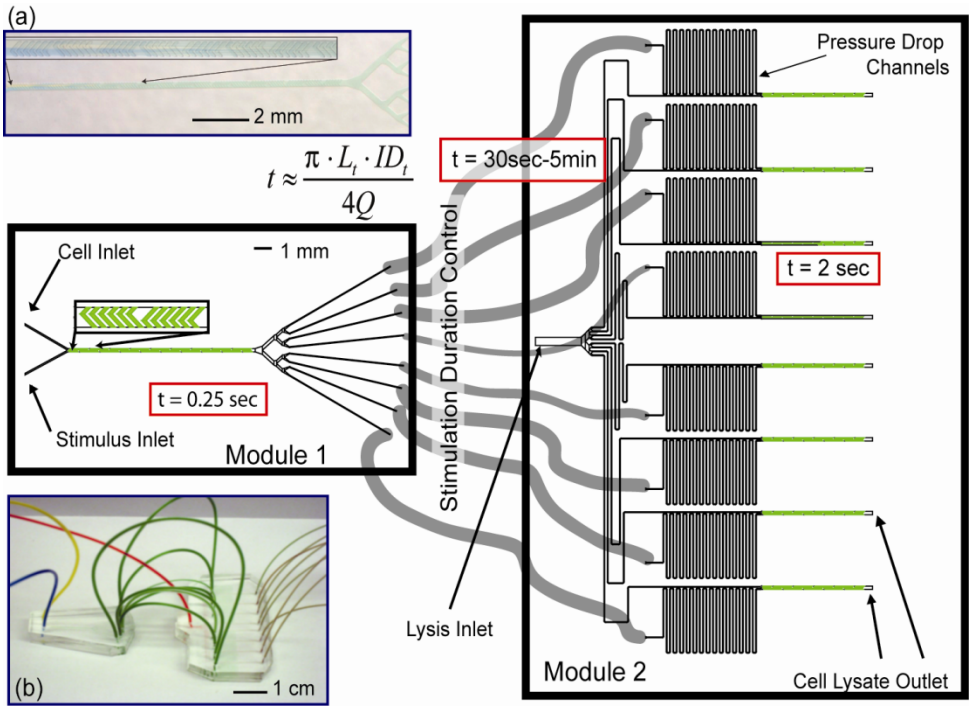

Figure 2-1 A schematic of the two module devices showing inlets, tubing, pressure drop channels and cell lysate outlets for sample collection. The respective residence times (*t*) in each unit are noted in red boxes on the figure, where the total time is essentially the time in the tubings, varying with length (*L*), inner diameter (*ID*) and volumetric flow rate (*Q*). Insets (a) shows a close-up of Module 1 and (b) the whole device setup.

This modular design, as shown in Figure 2-1, created a more flexible system by using interchangeable tubing of different lengths and diameters for multiple time point options. The majority of the incubation time occurred in the interchangeable tubing. However, the flow rates must not be influenced when changing lengths or diameters of tubing. This is inherent in our system design because of the small dimensions of the microfluidic channels and the d^4 dependence in the denominator in Equations 1 and 2. In the worst case scenario with dimensions used in our experimental setup, the channel resistance was still four orders of magnitude greater than that of the tubings. Furthermore, additional long pressure drop channels were added to increase this effect. Small variations in the channel dimensions in the PDMS molding should not affect our flow distribution and residence time predictions. Since each time point channel has the same dimensions the major importance realizes in the relative difference between the channels and tubing. This order of magnitude effect will not be influenced by micron variations in PDMS molding. To ensure this premise holds, the flow rates at each outlet were measured experimentally.

2.3 Materials and methods

2.3.1 Device fabrication

This two-module device was fabricated using standard soft lithographic techniques [69]. Briefly the modules were molded in poly(dimethyl-siloxane) (PDMS) (Dow Corning Sylgard 184, Essex-Brownwell Inc., McDonough GA) from a two-layer SU-8 (Microchem Corp., Newton, MA) master. One layer of 50 μm thick SU-8 2050 was spun onto 100-mm silicon wafer, baked, and exposed under UV light to define a

negative image of the channel system in the resist. After baking to crosslink the exposed resist, another layer of 15 μm thick SU-8 2010 was spun on top. This layer formed the staggered herringbone array. After the same bake and expose process, the wafers were developed using propylene glycol monomethyl ether acetate (Doe & Ingalls, Inc., Durham NC). The wafer was surface-treated with vapor-phase tridecafluoro-1,1,2,2-tetrahydrooctyl-1-trichlorosilane (United Chemical Technologies, Inc, Bristol PA) for surface passivation. Then PDMS was cast on the SU-8 master and baked for 2 hours at 70 ^{o}C. The PDMS was peeled off the mold and individual devices were cut to size. Medical grade polyethylene (PE) tubing (Scientific Commodities, Lake Havasu City, AZ) of various lengths and inner diameters were used to for fluidic connections. Holes for fluidic connections were punched to a size determined by the outer diameter of the appropriate tubing.

2.3.2 Device operation

A syringe pump (Harvard Apparatus PHD 2000 Series Infusion) controlled the flow to the 3 inlets at 28.22 μL/min resulting in a 1/2 dilution of the stimulus and a 1/3 dilution of the lysis buffer. Because of this, the stimulus and lysis buffer were delivered at 2x and 3x concentration, respectively. The input cell concentration was ~8x10^{6} cells/mL. The resulting sample flow rates were 10.6 μL/min. For negative control, cell culture medium was first used in the place of the stimulation solution. After the start of the flow, the fluid was flushed to waste for 9 minutes before sample collection. The time corresponded to that for the fluid front to get from the syringe to the end of the outlet tubing. The sample lysate effluent was collected for approximately 15 minutes to obtain 150 μL of sample, enough to perform all downstream analysis. To stimulate the cells, the

process was repeated, with 2 μg/mL OKT3 antiCD3 diluted in media in place of cell culture medium inlet. The total amounts of reagents used for all 8 time-point sample collections included only 1.35 mL of cell suspension and lysis buffer, and 0.68 mL of media and stimulus. With improvements on the sensitivity of downstream analysis it is possible to collect far less lysate, thus conserving valuable sample.

Cells tend to settle over time because they are denser than the media that they are suspended in. The settling in the syringes and tubings causes cell loss during experiments and unreliable time data. Settling in the microfluidic channels causes the cells to roll along the bottom of the channel rather than follow the streamlines. To resolve this issue, the media and stimulation solutions were supplemented with dextran of ~70,000 MW (Sigma-Aldrich) to match the density of the cells (approx. 1.07 g/cm^3). The cell distribution after Module 1 was characterized by using only Module 1 with one inlet flowing medium containing cells at a know concentration and the other medium, both supplemented with dextran. The suspension in each outlet was collected and cells were counted to determine cell concentration.

2.3.3 Residence time distribution (RTD) experiments

RTD experiments were performed with 10 μm fluorescent tracer beads. A router with two inputs, one density matched carrier medium (dextran to 1.062 g/cm^3 to match density of polystyrene beads) and the other beads suspended in carrier medium. The router outlet was attached to specific tubing whose length and diameter were dictated by the desired residence time. That tubing leads into another microfluidic device containing a straight channel used for imaging. During normal operations the router valves were actuated such that beads were directed to waste and carrier fluid was sent through the

tubing. Then, at time zero, the valves were actuated to redirect flow of beads to the tubing for a few seconds. Then the valves were returned to normal operation, resulting in a short spike of tracer beads. During experiment, images were captured every 250 ms in the channels directly before and directly after the tubing. MATLAB was used to count the number of beads in each image, the time course was binned into sections of 10s to create a histogram.

2.3.4 Confocal microscopy

The confocal experiments were performed on a LSM 510 UV microscope (Carl Zeiss Inc) with a 20x lens. Rhodamine-B dye at 0.05 mg/mL was used in one of the two entering streams. Inlets were perfused with the same flow rate as experimental conditions. The mismatch viscosity was created by using solutions of sucrose in water [70].

Excitation was from a helium-neon laser (543 nm, 0.5 mW) and emission at 560 nm using a long pass wavelength filter optimized for Rhodamine-B. The pixel time was 1.6 μs with 2-μm slices in the z plane. Confocal images were used to evaluate the extent of mixing. After each cycle the standard deviation (σ) of intensity distributions of the channel cross-sections. A σ value of 0.5 signifies completely unmixed streams while a 0 value signifies completely mixed streams. For figure clarity the brightness and contrast were increased in the same way for all x-y projections.

2.3.5 Computational fluid dynamic models for the chaotic mixer

We modeled the transport and mixing in the SHM using the 3-D Navier-Stokes equations for flow and the diffusion-convection transport equation for the stimulant and the lysis buffer components at steady state. These equations were solved using

COMSOL. Because of the asymmetry in the SHM, the model could not be reduced. However, the Navier-Stokes and convective diffusion equations can be decoupled and were solved separately. The vector form of the Navier-Stokes equations was as follows:

$$\rho \frac{\partial \mathbf{u}}{\partial t} - \mu \nabla^2 \mathbf{u} + \rho(\mathbf{u} \cdot \nabla)\mathbf{u} + \nabla p = F \quad (5)$$

where ρ is the density, μ is the viscosity, $\boldsymbol{u}$ is the velocity vector, p is pressure, and F is a volume force field (gravity). This solver assumes incompressible flow ($\nabla \cdot \mathbf{u} = 0$). The boundary conditions were assigned as parabolic flow profiles at a given average velocity for the inlets, zero pressure at the outlet, and non-slip on all remaining exterior boundaries. The interior boundaries were all assigned a neutral condition. These interior boundaries were created for enhanced 3-D mesh resolution by splitting the flow channel into 8 subdomains and the herringbones into 6 subdomains each. This created additional nodes inside the subdomain while allowing a continuous solution to the Navier-Stokes equations. The mesh density was increased until further changes did not affect the solution. The final mesh consisted of 65,000 elements with and an average mesh quality of >0.3.

Then using the velocity field from the solution of the Navier-Stokes equations, the non-conservative convective diffusion equations were solved

$$\delta_{ts} \frac{\partial c}{\partial t} + \nabla \cdot (-D \nabla c) = R - \mathbf{u} \cdot \nabla c \qquad (6)$$

where δ_{ts} is the time-scaling coefficient, equal to 1 when solving in the seconds timescale (this term will drop out at steady state), c is the concentration, D is the diffusion coefficient (~1×10^{-11} m^2/s for protein molecules[71]), R is the reaction rate (set to zero in our model), and $\boldsymbol{u}$ is the 3-D velocity profile from the Navier-Stokes equations. The

boundary conditions were assigned as $c = 1$ and $c = 0$ at each inlet, convective flux at the outlet, and insulation at all remaining exterior boundaries. The interior boundaries were all assigned a continuity condition.

2.3.6 Cell culture, cell lysis and protein analysis

For this study, we used Jurkat E6-1 human acute T-cell lymphoma from ATCC (Manassas, VA, USA). Cells were cultured in RPMI 1640 medium with L-glutamine (Sigma- Aldrich) with 10 mM HEPES, 1 mM Sodium Pyruvate, and 1X MEM Nonessential Amino Acids, and 100 units/mL penicillin streptomycin (Cellgro), supplemented with 10% certified heat inactivated fetal bovine serum (Sigma-Aldrich) at 37 ^{o}C in a humidified 5% CO_2 incubator. For the experiments, Jurkat cells were resuspended in a phenol-red free RPMI 1640 medium (Sigma-Aldrich), supplemented with the previous reagents and 0.3 mg/ml of L-Glutamine (VWR) and 7 wt% dextran (Sigma-Aldrich). For the cell signaling experiments, the cells were treated with anti-human CD3, clone OKT3 (eBioscience) at a final concentration of 2 μg/mL. The lysis buffer used in these experiments was based on a 1% NP-40 solution (USBiological), supplemented with 1 M β-glycerophosphate (Calbiochem), 0.2 M sodium pyrophosphate (Alpha Aesar), 1 M sodium fluoride (EMD), 5 M Tris (Promega), 0.2 M sodium orthovanadate (Alfa Aesar), 5 M sodium chloride (Alfa Aesar), 100 mM benzamidine (Sigma), 500 mM EGTA (VWR), 5 mg/ml aprotinin (Sigma), 5 mg/ml leupeptin (VWR), 1 mg/ml pepsatin (Sigma), 1 mg/ml microcystin-LR (Sigma). For device-mediated cell lysing, lysis buffer at 0 °C was directly mixed with the cell suspension in Module 2 and lysate solution collected at the outlets of the device in microcentrifuge tubes. For standard bench lysing, the addition was made by pipette addition of lysis buffer to microcentrifuge

tubes containing the cells. For both forms of lysing, the samples were incubated on ice for 10-30 minutes, centrifuged at 14,000 rpm for 10 minutes and the supernatants were used for further analysis. The total protein concentration after lysis was determined with a BCA assay kit[72] and results were obtained after protein content between samples was diluted to uniform levels.

2.3.7 Stress and signaling

All analysis of phosphorylation dynamics were performed with a Bio-Plex-200 instrument (Bio-Rad) using commercially available Luminex bead assays. The phospho-JNK and phospho-p38 measurements (BioRad) or the quantification of proteins downstream of TCR (Beadlyte 7-plex Human T-Cell Receptor Signaling Kit, Millipore) were completed according to manufacturers' protocols. Results for all data are presented as the average of three independent sets of experiments. To adjust for baseline changes between experiment days, mean fluorescence intensity for each protein assay across samples was normalized by the maximum value for the data.

2.4 Results and discussion

2.4.1 Analysis of rapid mixing by microscopy and computational methods

The CFD modeling results and confocal images from experiments are shown in Figure 2-2. In the confocal images (Figure 2-2 c and d), the bright fluorescent fluid is analogous to a stimulus rich solution and the dark areas is analogous to fluid with no stimulus. The experimentally determined profiles are similar to those by Stroock *et al.* under the same conditions. More importantly, the computational model agrees well with

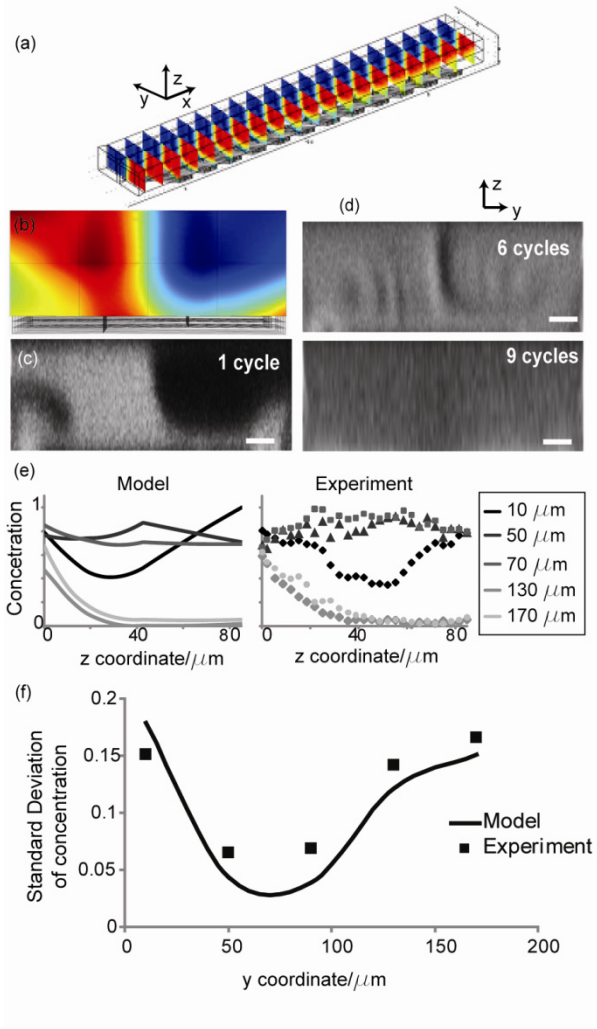

Figure 2-2. Comparison of COMSOL model results with experiment. (a) Perspective view of the mixing for 1 cycle of herringbone mixers. The slices are in the y-z plane perpendicular to the direction of flow. (b) y-z plane of the concentration profile color map from the model after 1 cycle. Under the color map the z component of the herringbones are illustrated. (c) y-z view of a confocal image of mixing after 1 cycle with one inlet containing rhodamine dye. (d) y-z mixing profile after 6 and 9 cycles. The scale bar is 20 μm, twice the average diameter of a T-cell. (e) Comparison of mixing profiles at in the cross section. Each line represents the normalized concentration profile in the z direction at the designated distances in the y direction from the wall. (f) Standard deviation of concentration across each line in (e).

experimental data (Figure 2-2 e and f); hence the models can be used as a tool to probe the mixing properties and factors that may influence the extent of mixing to optimize our experimental conditions. Experimental results for mixing of solutions with the same viscosity (mimicking cell and stimulus mixing conditions) suggest that most cells would come into contact with the stimulus after 6 cycles because the widths of the stimulus-negative solution stream are smaller than the cell diameter (~ 10 μm); the standard deviation of mixing is 0.14. After 9 cycles the solutions are completely mixed with a standard deviation of 0.05.

In contrast, when solutions with mismatched viscosity and density are mixed (as in the case of mixing cell suspension, $\mu \sim 4.3$cP and $\rho = 1.07$g/cm^3, with lysis buffer, $\mu \sim 2.4$ cP and $\rho = 1.06$ g/cm^3) with the same SHM, as seen in Figure 2-3, the streamline profiles and hence the extent of mixing are qualitatively different. In this case, the mixing is slower and less efficient, marked by incomplete mixing after 9 cycles in a

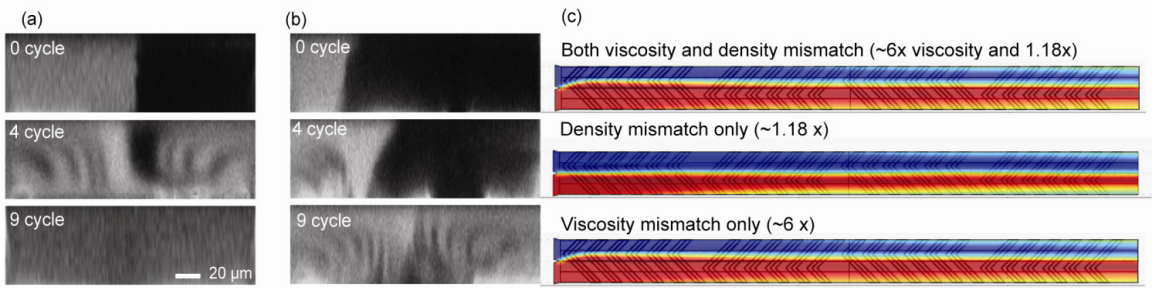

Figure 2-3. Comparison of mixing of different viscosity solutions. (a-b) Confocal images of the cross section at increasing mixing cycles of herringbones. One inlet contains fluorescent rhodamine dye. (a) y-z cross-sectional view of the mixing of two fluids with the same viscosity. (b) y-z cross-sectional view of the mixing of two fluids with mismatched viscosity; the fluid with no fluorescent dye has a viscosity 20 times the other. (c) Top view in the x-y plane of COMSOL data for density and viscosity mismatched solutions. The viscosity and density values are based on the sucrose solutions used with 6x the viscosity of water.

mixing of solutions of 20 times viscosity mismatch. The standard deviation was 0.12. Although the viscosity and density of fluids are correlated in most cases, we can separate the two effects in the numerical simulations. Our models suggest that less effective mixing is mainly due to the mismatch in viscosity, not the difference in density, because the more viscous solution has a lower average velocity and therefore takes up more cross-sectional area (Figure 2-3c). This results in the fluid interface moving beyond the point of asymmetry (2/3 of the way across the channel) of the herringbones, reducing the effectiveness of the herringbones' ability to stretch, fold, and mix the two fluids. However, this effect occurs only at viscosity ratio of 6:1 and above for the current SHM design. Because we use dextran-supplemented solutions, we stay below the 6:1 viscosity ratio and therefore the SHM is adequate for fast mixing of cells and stimulus in Module 1, and of cells and lysis buffer in Module 2.

The model was also used to characterize the shear stress at the walls. At the channel wall highest shear stress is 6 Pa and the highest shear stress at the herringbone wall is 1.8 Pa. These numbers are on the same order as the in the blood, with maximum shear stress of approximately 4 Pa [73].

2.4.2 Tight control of stimulation times in multiple parallel samples

Based on the channel dimensions and fluid flow rates of the optimized setup, the staggered herringbone array achieved full mixing of reagents with minimal shear in less than 0.2 seconds on the stimulation chip (Module 1), and <0.9 seconds on the lysis chip (Module 2). These times are less than 5 percent of the ~23-second stimulation time,

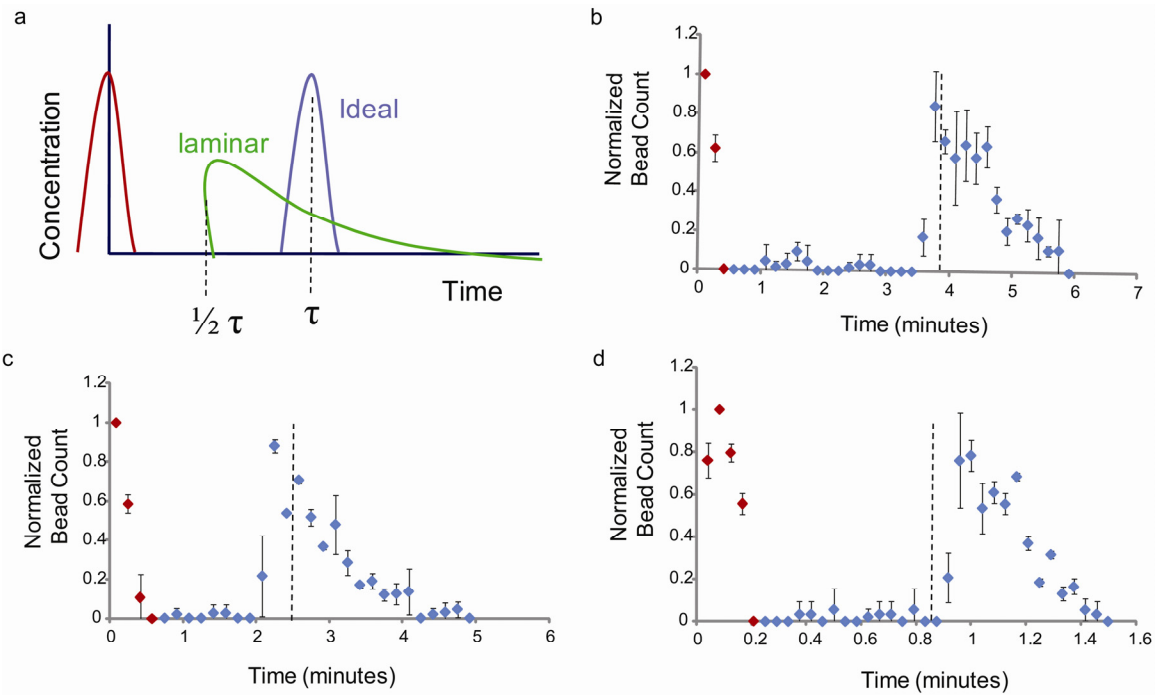

Figure 2-4. Residence Time Distribution (RTD) data. a) Shows the expected trends for a plus input (blue). For an ideal plug flow the red peak would appear at the outlet at the expected space time (τ). A perfect laminar flow profile is shown in green. b-d show data for different expected space times. The blue is the RTD before the tubing and the red is in the channel after. b) τ = 4.2 minutes, c) τ = 2.5 minutes and d) τ = 1 minutes. The experiment in (b,c) were performed using PE tubing with the ID 0.58mm and the experiment in (d) was using PE tubing with the ID 0.38.

which was the shortest stimulation time in our experiments. Hence the mixing time does not significantly affect our time point data.

Taylor dispersion, caused by diffusion and the parabolic flow profile, could be important for the cell stimulation time. With a diffusion coefficient on the order of $1x10^{-10}$ cm^2/s (from Stokes-Einstein's equation), the modified Peclet number (ratio of the shortest residence time to the timescale for dispersion) is on the order of $1x10^5$, suggesting Taylor dispersion will affect the stimulation/incubation time distribution. Residence time distribution (RTD) experiments were performed to determine the extent of dispersion present for the cells flowing in the PE tubing. Figure 2-4 shows the RTD

data. While the distribution does not exhibit ideal plug flow behavior for the given residence times, the distribution is far more uniform around the desired residence time than perfect laminar flow would predict.

Table 2-1. Example tubing dimensions for given time points and the pressure drop (analogous to resistance) for each tubing.

Time point/min	Tubing ID/mm	Tubing Length/cm	ΔP/Pa
0.5	280	4.2	66.4
1	380	4.7	21.9
1.5	580	3	2.6
2	580	4.1	3.5
2.5	580	5.2	2.6
3	580	6.2	3.
4	580	8.3	4.2
5	580	10.4	5.3

2.4.3 Flow resistance balance to achieve equal distribution of fluids

The flow rate in each outlet was characterized as described in the experimental methods section. Figure 2-5a shows the flow rates across different time points with varying tubing dimensions. Error bars represent the standard deviation from trial to trial, which demonstrates the repeatability from device to device. The flat trend and tight standard deviation around the target 8.3 μL/min flow rate demonstrates the reliability of the device flow rates even while varying length, widths, and thus resistance of the tubing (as shown it Table 1) between Modules 1 and 2 for each point. The pressure drops in the highest pressure drop in the tubing is 66 Pa vs. 18 kPa in the microfluidic channels. The

advantage is that this configuration provides large flexibility of the specific time points for stimulation we can achieve. With commercially available tubings, we can easily achieve stimulation times of ranging from ~20 seconds to 1 hour.

2.4.4 Reliable cell distribution after stimulation and reliable protein yield after lysis

Without adding dextran to the cell suspension, cells were often observed to settle and aggregate; these aggregations in turn cause blockage on chips and together with settling cause the cell distribution in the 8 collected samples to be non-uniform and unpredictable. In comparison, reliable cell distribution between experiments was achieved by adding dextran to the solutions for density matching. In addition, dextran may also contribute to the suppression of non-specific adsorption of serum proteins in the medium, which promotes cell adhesion to the device walls. As shown in Figure 2-5b, the average standard deviation of cell density in each stream was decreased by more than half. These data were obtained by flowing cells through the device at a known density, but replacing the stimulus and lysis solutions with media, and counting intact cells from each outlet. In addition, by taking the cells lost (Figure 2-5c) to settling in the syringes and devices into account, the resulting improvement by adding dextran is very significant. Although variability between cell concentrations per stream still exists (and this issue will be addressed in later chapters), protein activity data can be easily normalized by the total protein in the sample. We have verified that the total protein yield is linearly correlated to the number of cells in the sample (data not shown).

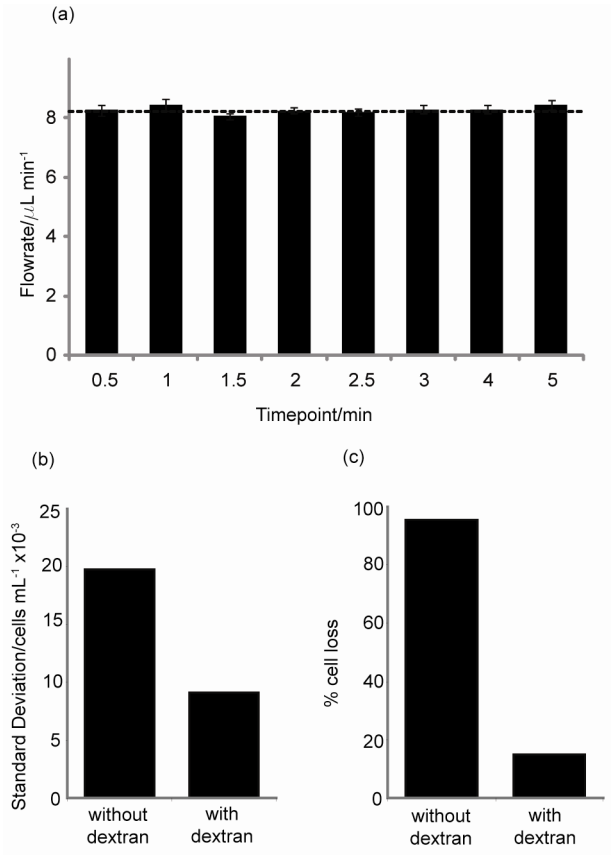

Figure 2-5. Demonstration of device uniformity. (a) Equal flowrates in μL/min across the different channels. The channels are noted with the corresponding stimulation time in minutes. The dashed line indicates the set flow rate (total/number of channels) and error bars indicate standard deviation**.** (b) The average standard deviation of cell concentration in each stream with and without dextran supplement in the solutions. The standard deviation between experiments is decreased by half with the addition of dextran and percent cell loss is markedly decreased.

2.4.5 On-chip cell handling showing minimal stress on cells

For a microfluidic device to perform optimally for signal transduction applications, fluid forces must not impose adverse stresses on the cells within the chip. To validate that the cells flowing through the device were not subjected to undesirable shear stress due to fluid flow in narrow channels, undesirable mechanical forces produced by chaotic mixing, or lack of oxygen perfusion during the course of the experiment, the

phosphorylation state of two MAPK proteins associated with stress response, p38 and JNK, were monitored. Cells in dextran-supplemented medium (no stimulatory reagents) were pumped through Module 1 and lysed in Module 2. The lysates were compared to the results from cells lysed by an analogous bench-top protocol (also without any stimulation). As shown in Figure 2-6, the levels of p38 and pJNK activation for the on-chip experiment are constant over time and comparable to the results obtained on bench, demonstrating that the cells are neither adversely stressed by the conditions imposed by flow through the microchannels, nor stressed by the time spent in the tubings. There was no noticeable change in cell viability or morphology as observed by trypan blue exclusion after cells were subjected to flow through the device (data not shown).

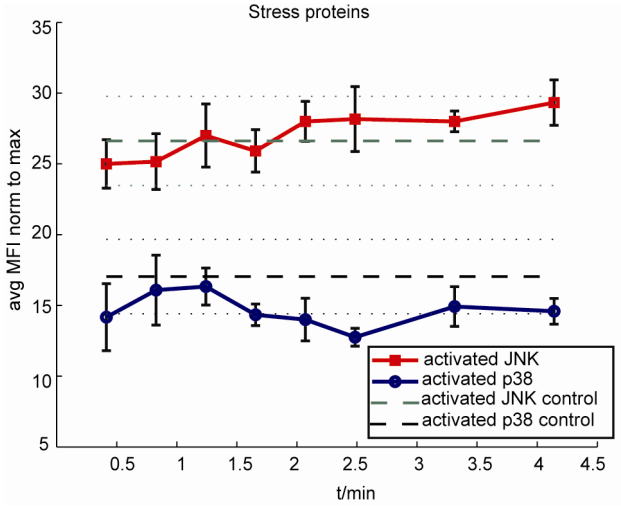

Figure 2-6. Stress protein activity in device. Activated JNK and p38 concentrations in cells collected from the microfluidic devices compared to on bench controls, showing no signs of cellular stress induced by the device. For this experiment, samples were normalized to total cellular protein content. The experiments were run with three different devices and then the protein phosphorylation quantification was obtained with duplicates. Dashed lines represent the quantified values for phospho-p38 and phospho-JNK from control samples lysed on the bench. Dotted lines indicate standard deviation associated with the control values.

2.4.6 Parallel on-chip experiments for high-throughput multi-time point protein activation assays

The temporal regulation of protein activation during T-Cell receptor signaling involves multiple coordinated feedback loops, as reviewed by Germain *et al.*[17]. Prior proteomic studies indicate widespread phosphorylation of signaling molecules occur within 5 minutes of T-Cell activation [18]; thus, a method for consistent generation of sub-minute signaling events would be useful for extracting relationships between interconnected network components. To ensure that the microfluidic system is a reliable method of evaluating T-Cell activation, we characterized the phosphorylation dynamics of representative signaling molecules downstream of the T-Cell receptor (Figure 2-7a). Comparisons between anti-CD3 (OKT3) stimulated Jurkat lysates generated by standard bench-top protocol and those generated by the device were made using the Beadlyte 7-plex human T-Cell receptor phosphoprotein signaling kit (Upstate). This kit quantifies phosphorylated ITAMs (CD3), ZAP-70, Lck, LAT, Erk, and CREB using the Luminex instrument as described by Khan *et al* [74]. Jurkat cells in a 7% dextran medium were stimulated with the soluble form of anti-CD3 for the incubation times ranging approximately from 20 seconds to 4.5 minutes and then lysed with a cold lysis buffer containing phosphatase and protease inhibitors that prevent further biochemical events after lysis. Figures 2-7b-2-7g show the signaling dynamics for these 6 proteins of interest for lysates generated by the microfluidic device and for lysates generated on bench. As illustrated in the simplified scheme of the TCR signaling cascade (Figure 2-7a), the first proteins to be phosphorylated are CD3, Lck and Zap-70. Multiple signaling events occur before the downstream adaptor LAT, and the kinases Erk and CREB, are phosphorylated.

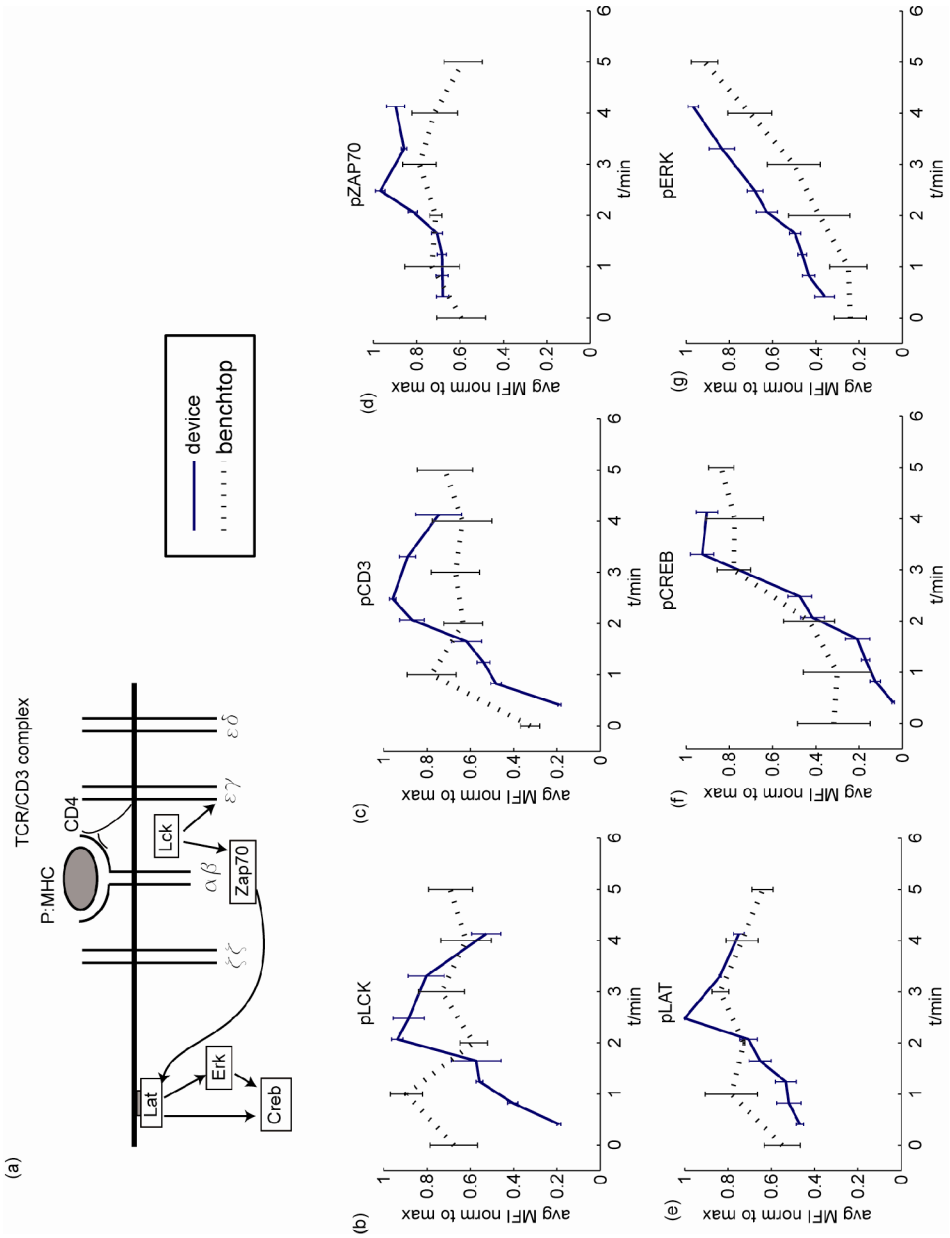

Figure 2-7. TCR activation dynamics (a) Simplified pathway of TCR activation. After a peptide MHC has bound to the CD3/TCR complex , Lck phosphorylates the ITAM CD3, that recruits the tyrosine kinase ZAP70 to the complex. Zap70 phosphorylates then the adaptor protein LAT that activates the MAPK and the Ras pathway, the latter enabling the activation of Erk and Creb. In our case, we used OKT3 that specifically reacts with the CD3 complex. (b-f) For each of the selected protein, comparison of the dynamics obtained with the microfluidic device and those obtained by standard bench top protocol. The device dynamics correlate to pathway order and the microfluidic device shows a better consistency in the results.

With the device, phosphorylation of CD3, Lck and Zap-70 starts after 2 minutes of stimulation and reaches its peak at 3 minutes. In contrast, the phosphorylation of Erk rises concurrently with the downstream protein Creb over a longer period of 5 minutes. As expected, smaller variation occurs among samples across repeated experiments with the microfluidic device than with the manual stimulation and lysing, demonstrating a tight control over cell handling on-chip. The dynamic trends of activation are not dissimilar between the two experimental methods; however, an important feature emerges from the data. The uniformity of stimulatory exposure results in higher magnitudes of phosphorylation at early time points for all proteins measured. This is especially evident in the CD3 ITAM phosphorylation, possibly due to a flattened distribution of stimulated cells in the manual bench-top samples arising from the time lag of antibody: cell mixing. This feature highlights the necessity of consistent sample handling when quantifying cell population averages for signaling dynamics, especially when using small numbers of cells.

2. 5 Summary

We present a two-module microfluidic platform for simultaneous multi-time point stimulation and lysis of T-Cells for early time point signaling activation with a resolution down to 20 seconds using only small amounts of cells and reagents. The key design features are rapid mixing of reagents and uniform splitting into 8 channels for simultaneous collection of multi-time point data. Chaotic mixing was investigated via computational fluid dynamic modeling, and was used to achieve rapid and complete mixing. This modular device is flexible - with easy adjustment of the setup, a wide range

of time points can be achieved. We show that treatment in the device does not elicit adverse cellular stress in Jurkat cells. The activation of 6 important proteins in the signaling cascade was quantified upon stimulation with a soluble form of α-CD3. The dynamics from device and conventional methods are similar, but the micro device exhibits significantly less error between experiments.

CHAPTER 3‡

SINGLE FIELD THREE DIMENSIONAL EPIFLUORESCENT PARTICLE IMAGINING TECHNIQUE

3.1 Overview

While many mixing devices, and our multi-time point stimulation device from Chapter 2, demonstrate many utilities, studying how and evaluating how well they work are mostly limited to two-dimensional imaging at present. Having three-dimensional spatial information is a necessary step towards designing the next generation mixers, separators and manipulators and improving their performances as particles may behave differently when flows are rotated, split, and combined. For our particular the objective is to develop a mixer that would result in a uniform cell distribution across all 8 outlets.

To address the need for imaging larger particles in a wide range of flow conditions, including complex flow patterns, we developed the simple Single-field Three-dimensional Epifluorescence Particle (STEP) imaging technique discussed in this chapter. This technique acquires images of fluorescent particles in a single-field, identifies the in-plane coordinates of those particles and uses the pattern of out of focus light to determine the particles' distance from the focal plane based on an empirical correlation. Unlike the optics theory approach, this empirical correlation also works for

‡ Manuscript under review, Lab on a Chip

fast flowing particles where the particle's fluorescence profile is smeared in the direction of flow. This technique can provide fast data acquisition with little computational burden, and only requires a widely available epifluorescent microscope.

3.2 STEP Principles

For STEP imaging, first, we observed that trajectories of moving particles in cross-section have similar intensity distributions as the cross-section distribution of a stationary particle at the same distance from the focal plane – z position (Figure 3-1 a,b). The fluorescence patterns of particles away from the focal plane evolve from a circular spot-like profile to a ring-like profile (Figure. 3-1c); note that the shape and spread (not intensity) depend on the z-position. These parameters are therefore independent of exposure time, light intensity, and particle velocity. For simplicity's sake, we fit the distributions to Gaussians, and the z position correlates well with either the standard deviation of a single Gaussian (σ) or the distance between the peaks of two Gaussians (d). (Other fitting functions work similarly.) The empirical correlation curve (Figure 3-1d) was made by imaging particles (attached to a moveable surface) at known distances above the focal plane (the top of the glass slide) at 5 μm increments, and is specific for our experimental microscopy and fluid/particle system. Calibration typically takes a few minutes and only needs to be done once per particle fluid combination. The calibration curve generated is specific to the refractive index of the carrier fluid used. In these bead experiments the carrier fluid is a 6% dextran solution in water. Therefore, the same fluid should be used in experiments as in calibration curve generation. Note that this technique

acquires 3-dimensional particle position information without having to image at multiple focal planes.

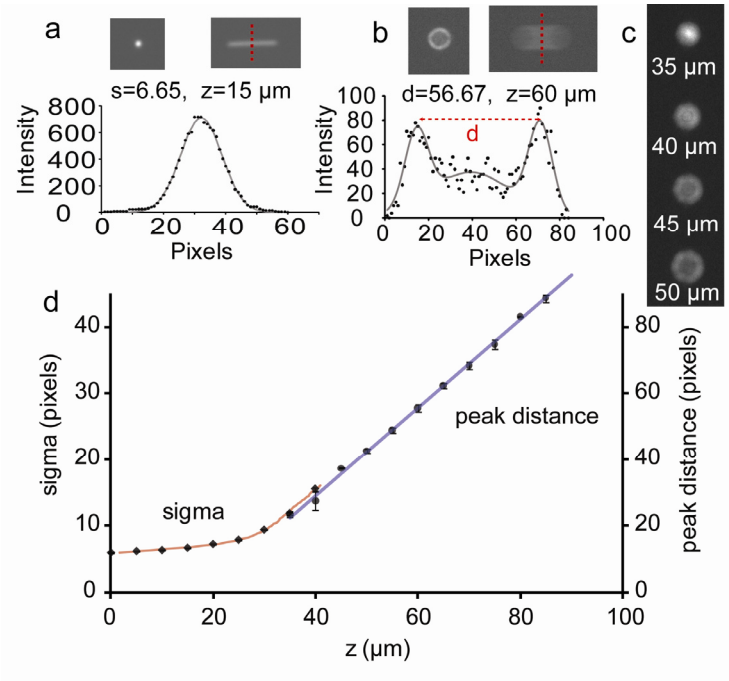

Figure 3-1. Principles of STEP imaging: (a-c) particle intensity patterns for 7.34 µm fluorescence particles in 6.5 wt/wt % dextran aqueous solution, using a 20x objective (NA=0.5). Examples of non-flowing (circular) and flowing (smeared) particles are insets; the line across the flowing particle indicates where the intensity distribution data is acquired. (a) Intensity distribution across a particle 15 µm from the focal plane. Gaussian distribution fit (grey curve) is quantified with standard deviation (σ). (b) The intensity distribution across the particle 60 µm from the focal plane. The Gaussians fits (grey curve) are quantified with distance between 2 peaks (d). (c) Images showing particles 35 µm to 50 µm from the focal plane. (d) The empirical fits to relate the standard deviation (σ) or peak distance (d) of the fitted intensity curves with the particle distance from the focal plane (z): $z = 0.7432 \cdot d + 183638$ or $z = 21.09 \cdot e^{0.04161 \cdot \sigma} - 8520 \cdot e^{-0.9696 \cdot \sigma}$, R^2 = 0.99 for both. Error bars represent standard deviation (n = 4). This empirical correlation is dependent on magnification, refractive index of the solution, particle size, emission wavelength, and thickness of the cover glass, and therefore is not universal. 1 pixel = 0.47 µm.

3.3 Materials and methods

3.3.1 Device fabrication

This device was fabricated using standard soft lithographic techniques [69]. The exact method was described previously [36]. Briefly the modules were molded in poly(dimethyl-siloxane) (PDMS) (Dow Corning Sylgard 184, Essex-Brownwell Inc., McDonough GA) from a two-layer SU-8 (Microchem Corp., Newton, MA) master. The channel layer was 70 μm tall and the groove layer was 20 μm tall on top of the main channel.

3.3.2 Device operation

A syringe pump (Harvard Apparatus PHD 2000 Series Infusion) controlled the flow to the 2 inlets at 33.3 μL/min. For particle studies one inlet contained a dilute suspension (0.1% volume fraction) of 7.34 μm fluorescent particles (Bangs Laboratories, Inc.™) in the carrier fluid (6.5 wt/wt% dextran in water) while the other inlet contained only the carrier fluid. The dextran was used to match the density of the fluid to that of the particles and eliminate density effects (settling or floating). For solute mixing the carrier fluid was 70 wt% glycerol solution, used to minimize diffusion effects. In this case, one inlet contained 0.01 mg/mL Rhodamine B (Sigma-Aldrich®).

3.3.3 Generation of calibration curve

The calibration curve was created as custom made mechanical set up as follows: A PDMS barrier pad was bonded to a glass slide such that the middle could be filled with the carrier solution. The glass slide was placed into a slide holder. Attached to the slide holder was a micrometer set up that held another glass slide with a PDMS pad attached to

it upside down over the initial glass slide. Fluorescent beads adhered to the PDMS slab (no treatment necessary because they naturally stick to the surface when the dextran solution is not used). Starting at the focal plane the micrometer was used to move the beads away at 5 μm increments while maintain focus at the top of the glass slide.

3.3.4 Image acquisition

Once the calibration curve was acquired, we imaged particle suspensions flowing through microfluidic systems (e.g. a slanted groove mixer (SGM) [37]). We took multiple epifluorescence images at a single fixed focal plane over time for statistical compilation of particle distribution. By using an objective with a large depth of field (e.g. 20x, NA=0.5), all particles within ~90 μm from the focal plane were captured. We optimized the exposure time, which is critical for effective image processing and quantification, so that there are no overlapping particle paths, the signal-to-noise ratio is maximized, and image saturation is avoided. Additionally, all experiments are performed in the dilute regime where the particle volume fraction is less than 0.1%. Therefore, given the flow rates and exposure time used, the occurrence of overlapping particles in images is negligibly small. In the case where particle-particle interactions are of interest, standard confocal techniques may be necessary [75, 76].

In a typical particle distribution experiment, 900 images are used to capture ~1000 fluorescent particles at volume fraction of ~0.1% at v_{avg} ~10 cm/s. We use Image-Pro (Media Cybernetics, Inc.) and a Hamamatsu EM C4742-95 camera (1-ms exposure, 9 fps). For the particle tracking experiments, we used Phantom v7.3 high speed imaging system (Vision Research, Inc.) with 1-ms exposure and 30 fps for a v_{avg} ~1 cm/s.

3.3.5 Image processing

To process data from each experiment, a custom image-processing program in MATLAB (Mathworks™) was used to translate the images into particle distribution maps (code located in Appendix B). This algorithm is accurate and simple (~5-10 min to process 900 images using a 2.39 GHz processor). A bright field image acquired at each imaging area was used to identify the y coordinates of the channel boundaries. For each experimental condition and imaging area (before any grooves and after each cycle), each image was processed using the following steps:

1) Read .tiff file into MATLAB as an *m* by *n* matrix, where *m* represents the *y* coordinates and *n* represents the *x* coordinates in pixels (x_{pix} and y_{pix}).
2) Subtract background.
3) Threshold image.
4) Clean image (clean, fill holes, etc.).
5) Identify individual particles and create a bounding box around each (shown as red boxes).
6) Identify the (x_{pix} ,y_{pix}) center of the box.
7) Draw a line from the x_{pix} edges of the box through the center (shown as dashed red line) and ± 1 pixel.
8) For each of the lines get the pixel values from the original image (before background subtraction).
9) Subtract background level from pixel values.
10) Fit each line to 3 Gaussians, find the distance between two furthest peaks (*d*) for each of the 3 lines, and take the average.

11) If d is greater than the threshold (where the correlation curve in Figure 3-1, changes from $z(\sigma)$ to $z(d)$), then use $z(d)$ to get the z coordinate.

12) If d is less than the threshold, fit each line to a single Gaussian, quantify with standard deviation (σ), take the average, then use $z(\sigma)$ to get the z coordinate.

13) To reduce noise, steps 7-12 were repeated for 2 additional lines, parallel to the original plus or minus 1 pixel in the x direction, and the z results were averaged.

14) Store the (x_{pix}, y_{pix}, z) coordinate. Note: (x_{pix}, y_{pix}) came from identifying the center of the bounding box and are in pixels, while the z coordinate is from the correlation curves and is in μm.

15) The pixel values were converted to μm using the channel boundaries identified from the bright field image. Figure 3-2 shows some images representing some of the above steps.

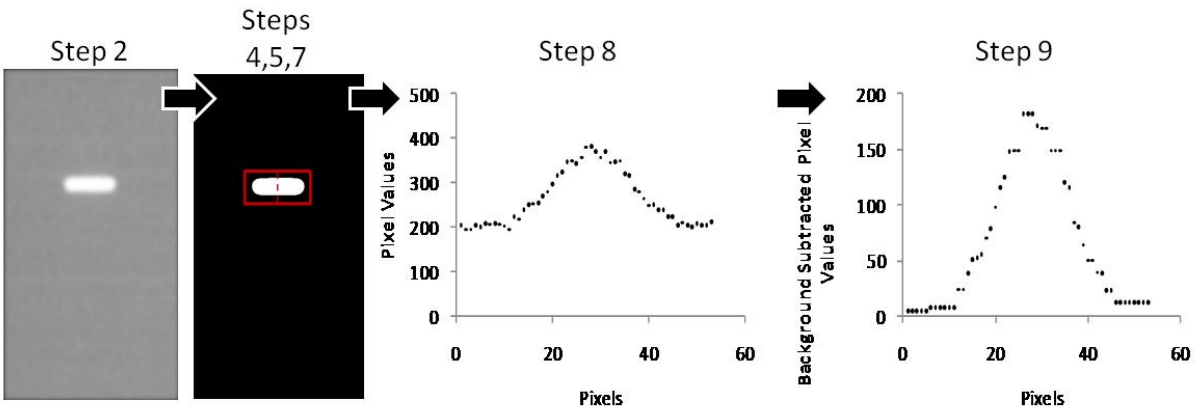

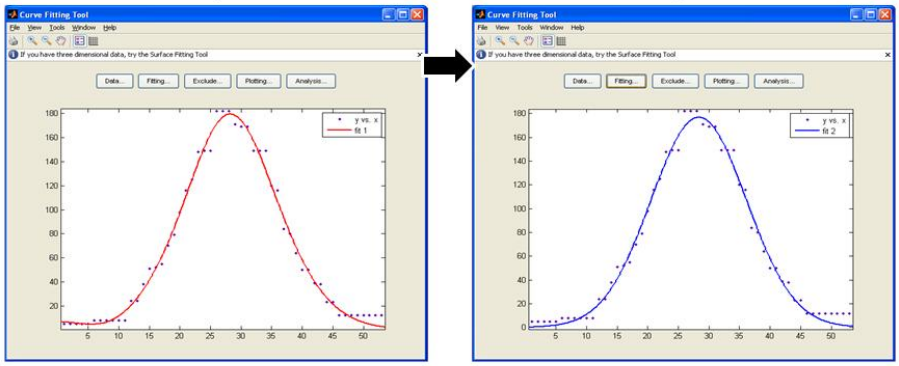

or

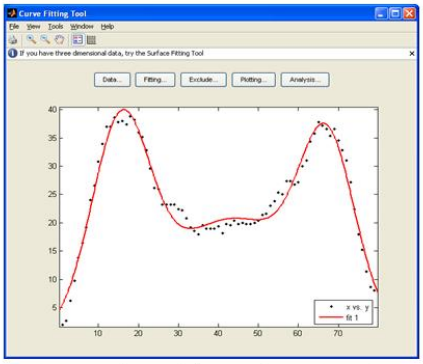

Figure 3-2. Steps in the MATLAB image processing.

After this process was completed for each image (typically 900 images per set) the results were plotted as concentration maps and scatter plots. For the concentration map, first a *m* by *n* matrix of zeros, where m is the width of the channel and *n* is the height of the channel, was created. Then, for each identified particle the value 1 was added at the specified (y, z) coordinate and each coordinate within specific particle radius, such that if 2 particles overlap, the value at the overlapping indices will be equal to 2. The result was in *m* by *n* matrix which when plotted gives a heat map of probably particle positions. The heat map image was saved as a .jpeg and the *m* by *n* matrix data was exported to an Excel file. Additionally, a scatter plot was generated with all the y-z data with each point represented by a circle relative to the particle size (in this case overlapping particle data was lost in the image). The scatter plot image was saved as a jpeg and the x-z coordinates were exported to Excel.

3.3.6 Confocal Microscopy

The confocal profile was generated from 8 rounds of volume scans (Zeiss LSM 510 UV, 20x, 0.78s exposure time, 2-μm steps in z) at the observation window; the volume was collapsed and projected onto the x-z plane.

3.4 Results and discussion

3.4.1 Method validation

To demonstrate STEP imaging's ability to resolve complicated flow patterns, we compared the distribution of fluorescent particles in an SGM imaged by STEP and by conventional confocal microscopy under the same flow conditions (Figure 3-3c). Because particles of interest are larger than the confocal's pinhole, confocal images cannot be

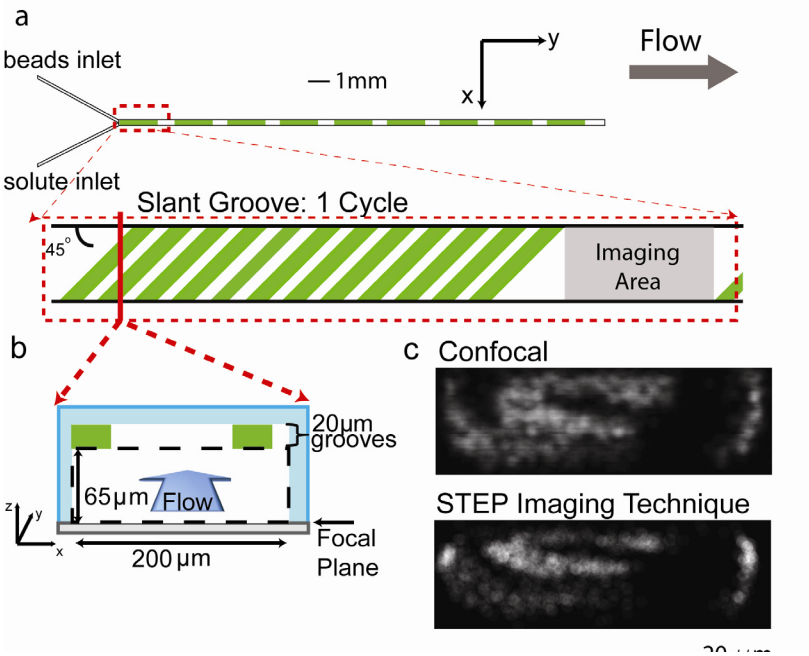

Figure 3-3. Imaging flowing particles in a slanted groove mixer. (a) The microfluidic device setup with a zoomed in section of one mixing cycle (12 grooves) for SGM. Channel is 200 µm wide and 65 µm tall; Grooves are 20 µm tall 50 µm wide, spaced 50 µm, and 45° relative the channel length. (b) Schematics showing the orientation of the imaging section with grooves on top of the channel, and glass slide on the bottom. The dashed box shows the area represented in distribution images. (c) The particle distribution in the channel cross-section after 7 cycles of SGM given by both confocal microscopy and STEP imaging. The experimental conditions in all experiments are the same: Re = 2 and particle Re = 0.01.

used to identify the center of mass (exact location) of individual particles or to track particles; it can, however, be used to generate probability maps. Probability maps describe only if a particle crossed that position at any point, it could be the center of the particle or the edge of the particle. Because these particles are large the error in the exact location of the particle is large. In contrast, the STEP imaging technique collects information from the whole volume in a single exposure, capturing the whole particle as it flows through the channel. Therefore, the exact location of the particle can be determined and individual particles can be recognized. Because the two techniques provide different types of data, it is not possible to directly compare them quantitatively.

However, qualitatively the two methods give similar distribution maps, demonstrating that STEP imaging is a viable alternative to confocal microscopy for studying three dimensional particle distributions. Additionally, because the coordinates of the particles are determined from curve fitting, the theoretical resolution of the STEP imaging technique is sub pixel in z.

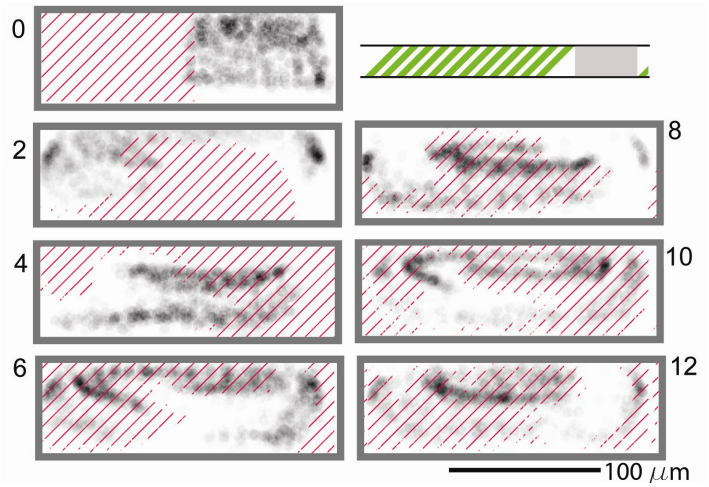

Figure 3-4. SGM-induced particle distributions in the channel cross-section for even cycles 0 - 12. The particle probability distribution pattern is in grey scale and solute distribution is indicated by red diagonal lines. The circulating pattern induced on particles from the slant grooves (shown as a top view) can clearly be seen here from cycle to cycle. Initially the particles and solute occupy opposite sides of the channel. The experimental conditions in all experiments are the same: Re = 2 and particle Re = 0.01.

3.4.2 Particle distribution patterns in complex flow

Figure 3-4 shows the particle distributions after a number of cycles in SGM. The circulating patterns of the particles induced by the grooves are clearly visible and easily discerned. For example, after 8 cycles, two circulating patterns can be seen. For comparison, solute mixing experiments at the same flow Reynolds number were

performed with confocal microscopy. The solute patterns were overlaid to the particle distributions. It is evident that solute and particles mix differently in this mixer, which highlights the need of such three-dimension imaging techniques that can be routinely used to study particle-fluid interactions in complex flow systems. We also observed relatively small deviations in the distribution between experiments, which reflect the deterministic nature of the laminar flow and the repeatability of our technique (Figure 3-5).

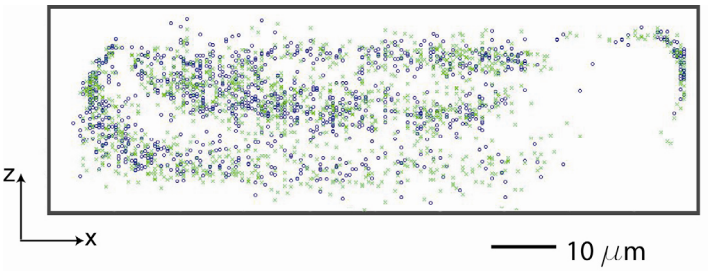

Figure 3-5. STEP imaging repeatability. The particle distribution at cycle 7 in the SGM from 2 independent experiments under the same flow conditions (Re = 2 and particle Re = 0.01). Particle positions are noted as blue circles in one experiment and green crosses in the other. This demonstrates the repeatability of our technique.

3.4.3 Particle tracking

Because STEP imaging technique can identify individual particles and their positions, particle tracking is also possible. In this case, images were taken with a high speed camera. The exposure time and frame rate were set such that, at a given flow rate, the particles in each image were practically circular, similar to stationary particles (i.e. direction of travel does not affect intensity profiles). Using the same method for particle position identification as in Figure 3-1, particles' *x, y, z* coordinates were computed. Our imaging condition also ensures that the same particles were clearly identifiable between

successive images. From the coordinate data between successive images, particle streamlines were constructed (Figure 3-6). Again, because we are operating in the dilute regime, typically only one particle is in the field of view at a time. This allows us to follow each particle easily from the time it enters the field of view until the time it exits. Evident from the figure, several particles move span-wise because of the presence of the grooves.

3.4.4 Trade-offs and limitations

In general, with increased camera sensitivity and/or particle brightness, STEP imaging technique could be extended to smaller particles or particles further from the focal plane. The trade-offs in experimental design are as follows: 1) The maximum flow rate is limited by the minimum exposure time and the field of view; the minimum exposure time is a function of the fluorescence intensity from the particle - brighter particles allow shorter exposure times, and thus faster flow rates. 2) The depth of field is limited by brightness of the particle and the numerical aperture of the objective. 3) The

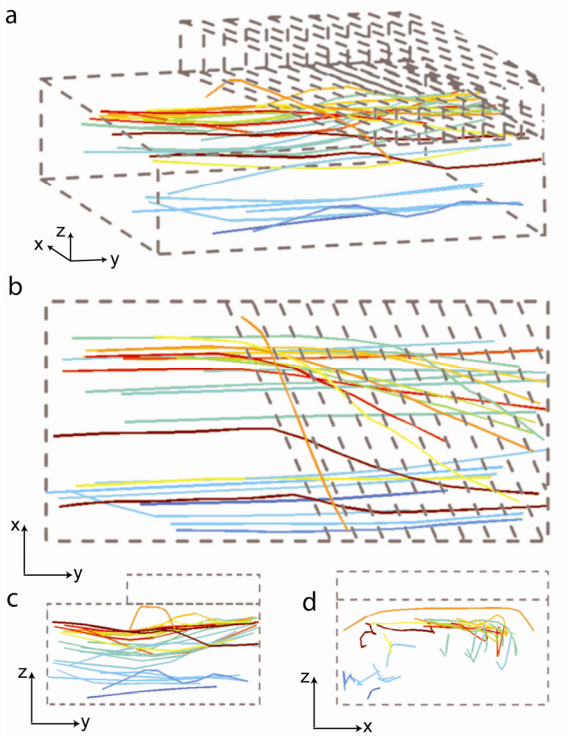

Figure 3-6. 3D particle tracking using STEP imaging. Tracking was performed in the SGM, at the end of the imaging area after cycle 2 into the beginning of cycle 3. In this experiment, 7.34 µm fluorescent beads were in both inlets, total flow rate 1 µL/min, exposure time 0.5 ms, and frame rate 30 fps. Colour indicates z-coordinate of initial particle position; blue (light) lowest, red (dark) highest.

minimum particle size is limited by pixel resolution, dictated by the camera pixel size and the objective in use, and camera sensitivity. For instance, using 0.47 µm per pixel as in this work, 1-2 µm diameter particles are the smallest possible to identify. Higher magnification could be used to identify smaller particles; however, one sacrifices the depth of field. At the limit where the particles become small enough that they can be assumed as a point source, µPIV techniques can be used [59, 60]. In this regime, the particles can be assumed to follow the streamlines and are therefore used to characterize the flow streamlines. The scope of our work is outside this regime, where the large particles do not follow the streamlines directly and optical theory cannot be easily used to predict the intensity pattern of the out of focus particles. 4) Also, camera quality must be

considered. If one used 8 bit camera instead, some resolution in intensity would be lost. This may limit the depth of field accessible and the minimum particle brightness one could practically use. 5) Finally, this technique can be extended to the use of cells (shown in Chapter 4). Neutrally buoyant suspensions were again created using dextran supplemented media, previously show to be compatible with cell based experiments [36]. Fluorescent labeling of the cytoplasm, using calcein for example, can be used to visualize the cells flowing through the device. Here the major limitation is in the size variation in the cell suspension. All cells will not have the same size, so the calibration curve is limited to the average size. Additionally, the uniformity of staining across the cell cytoplasm may not be perfect, resulting in additional error in fitting the intensity distribution. The result is a slightly less precise z position prediction

3.5 Summary

To the end of understanding flow of cells through complex 3-D flow schemes, we developed a Single-field Three-dimensional Epifluorescence Particle (STEP) imaging technique. This technique uses epifluorescent images of moving particles taken at a single focal plane and the pattern of out of focus light to determine the particles' distance from the focal plane based on empirical correlations. It is easy to use, requires only a conventional epifluorescence microscope, and yet provides single particle information faster and with potentially more spatial information than confocal microscopy. Using the STEP imaging technique, we are able to determine particle distributions and track individual particles in complex flow geometries.

CHAPTER 4

PARTICLE MIXING AND DEMIXING IN GROOVED CHANNELS

4.1 Overview

The staggered herringbone mixer (SHM, Figure 4-1a) was effective for mixing solutes (and bringing solutes to suspended cells) because in this device the two fluids are subjected to a sequence of rotational and extensional local flows that decrease the characteristic length for diffusion [37, 42]. However, we observed that for neutrally buoyant cells of finite size the distribution collected at the outlet, after 9 cycles of mixing, is dissimilar to that of the solutes and not uniform after long mixing time. This behavior was deterministic and highly reproducible (Figure 4-1b). This indicates a size dependence of particle distributions. Additionally, the groove geometry used was optimized for the mixing of fluids, which may not be the best to mix particles; it is possible that a different geometry would be better for mixing particles. Finally, although the inertial effects at high Reynolds number were ruled out, fluid Reynolds numbers in the experiments in Chapter 2 were on the order of 1, not a perfect Stokian flow. Therefore, we evaluated the effect of particle size, groove geometry and Reynolds number on the mixing of particles in grooved channel systems using the STEP imaging technique discussed in Chapter 3. The beginning of this chapter covers the dependence of particle distributions on particle size, groove geometry, and Reynolds number. The second part of this chapter covers a numerical model used to describe the observed particle distributions.

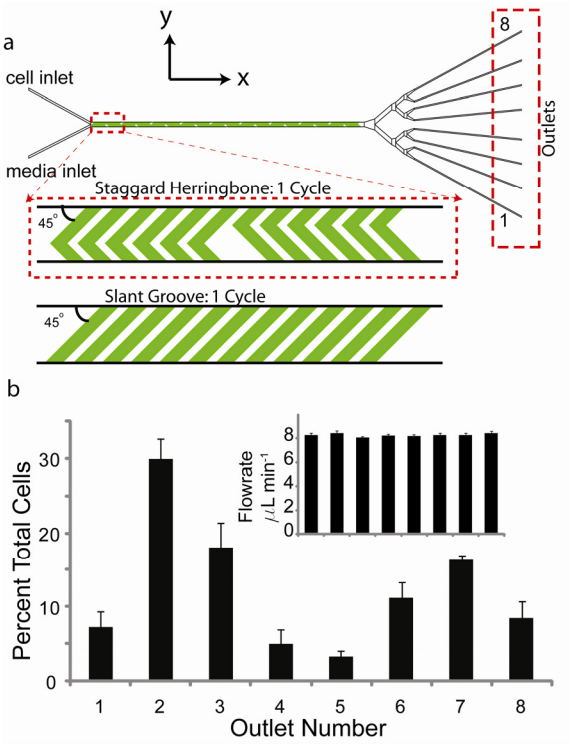

Figure 4-1. Cells do not mix as well as fluids in the Staggered Herringbone Mixer (SHM). While we were able to attain complete mixing of solute with the cells and distribute the fluids evenly between all 8 outlets, the cell distributions were consistently uneven. (a) The microfluidic device setup is shown with two inlets, one mixing channel, and 8 outlets. A zoomed in section of one cycle (12 grooves) of mixing is shown for both staggered herringbone grooves and the standard slant grooves. All grooves are 50 μm wide, 50 μm spaced, and 45 degrees relative the channel length. The mixing channel is 200 μm wide and 70 μm height with 20 μm deep groove on the top. Flow is in the x direction and the z axis in out of the page. (b) The cell distribution across the 8 outlets after 9 cycles of mixing is uneven, n=9 while the flow from each outlet is uniform (inset). Jurkat E6-1 human acute T cell lymphoma were used in these experiments.

4.2 Experimental material and methods

4.2.1 Device fabrication

This device was fabricated using standard soft lithographic techniques [69]. The exact method was described previously in Chapters 2 and 3 [36]. Briefly the modules were molded in poly(dimethyl-siloxane) (PDMS) (Dow Corning Sylgard 184, Essex-Brownwell Inc., McDonough GA) from a two-layer SU-8 (Microchem Corp., Newton, MA) master. The channel layer was 70 μm tall and the groove layer was 20 μm tall on top of the main channel (unless otherwise noted).

4.2.2 Device operation

A syringe pump (Harvard Apparatus PHD 2000 Series Infusion) controlled the flow to the 2 inlets at 33.3 μL/min. For particle studies one inlet contained a dilute suspension (0.1% volume fraction) of fluorescent particles (Bangs Laboratories, Inc.) in the carrier fluid (6.5 wt/wt% dextran in water) while the other inlet contained only the carrier fluid. The dextran was used to match the density of the fluid to that of the particles and eliminate density effects (settling or floating). For solute mixing studies the carrier fluid was a viscous 70 wt% glycerol solution, used to minimize diffusion effects. In this case, one inlet contained 0.01 mg/mL Rhodamine B (Sigma-Aldrich®).

4.2.3 Bead experiments

Using our STEP imaging technique from Chapter 3 we probed the effect of groove geometry, particle size, and Reynolds number (flow rate) on neutrally buoyant particle distributions. Unless otherwise noted, for consistency, all experiments were performed with the dextran supplemented carrier fluid in the inlet at y=0 μm and the bead

suspension was introduced in the second inlet at y=200 μms, and with one outlet after all the grooved cycles. The full set of variables probed is listed in Table 1. The fluid Reynolds number was varied over 3 orders of magnitude (0.02, 0.2 and 2) by varying the flow rate, four different bead sizes were used (4, 7, 10 and 15 μms), and four different grooved geometries were used. The base-case grooved geometries were the SHM and the simpler slant groove mixer (SGM). These grooves are 50 μm wide, 50 μm spaced, and 45 degrees relative the channel length. The mixing channel is 200 μm wide and 70 μm tall with 20 μm tall groove on the top. Two additional SGMs were used, one with taller grooves (50 μm tall instead of 20 μm tall) and one with wider grooves (100 μm wide instead of 50 μm wide and spaced 100 μm wide instead of 50 μm). The 4, 7, and 15 μm beads were green fluorescent (Bangs Laboratories, Inc.) and the 10 μm beads were red fluorescent (Invitrogen). For image acquisition we used a 20x air objective (NA 0.5), Image-Pro (Media Cybernetics, Inc.) and a Hamamatsu EM C4742-95 camera (10-ms exposure, 9 fps).

Table 4-1. Experimental variables.

Variables (units)	Values
Reynolds number	0.02, 0.2, 2
Particle size (μm)	4, 7, 10, 15
Groove geometry	SHM, SGM (standard, taller grooves, wider grooves)

4.2.4 Cell experiments

Jurkat E6-1 human acute T-cell lymphoma from ATCC (Manassas, VA, USA) were used in cell distribution experiments and imaged using the STEP imaging technique

from Chapter 3. Cells were cultured in RPMI 1640 medium with L-glutamine (Sigma-Aldrich) with 10 mM HEPES, 1 mM sodium pyruvate, and 1X MEM Nonessential Amino Acids, and 100 units/mL penicillin streptomycin (Cellgro), supplemented with 10% certified heat inactivated fetal bovine serum (Sigma-Aldrich) at 37 ^{o}C in a humidified 5% CO_2 incubator. For the experiments, Jurkat cells were resuspended to a concentration of 1 million/mL in medium , supplemented with the previous reagents, 7 wt% dextran (Sigma-Aldrich) and 1 μM calcein (Invitrogen). They were incubated for 45 minutes prior to injection into the device. Cell distributions were analyzed for a subset of the bead experimental conditions listed above. For image acquisition we used a 20x air objective (NA 0.5), Image-Pro (Media Cybernetics, Inc.) and a Hamamatsu EM C4742-95 camera (10-ms exposure, 9 fps).

4.2.5 Confocal microscopy

The confocal experiments were performed on a LSM 510 UV microscope (Carl Zeiss Inc) with a 40x oil lens. Rhodamine-B dye at 0.05 mg/mL was used in one of the two entering streams. Inlets were perfused with the same flow rate as experimental conditions. Excitation was from a helium-neon laser (543 nm, 0.5 mW) and emission at 560 nm using a long pass wavelength filter optimized for Rhodamine-B. The pixel time was 1.6 μs with 2-μm slices in the z plane.

4.2.6 Plotting particle/cell density distribution data

For the concentration map, first a *m* by *n* matrix of zeros, where *m* is the width of the channel and *n* is the height of the channel, was created. Then, for each identified particle the value 1 was added at the specified (*y, z*) coordinate and each coordinate within specific particle radius, such that if 2 particles overlap, the value at the

overlapping indices will be equal to 2. The result was in *m* by *n* matrix which when plotted gives a heat map of probably particle positions. The heat map image was saved as a .jpeg and the *m* by *n* matrix data was exported to an Excel file. Additionally, a scatter plot was generated with all the (*y,z*) data with each point represented by a circle relative to the particle size (in this case overlapping particle data was lost in the image). The scatter plot image was saved as a jpeg and the (*y,z*) coordinates were exported to Excel.

4.3 Results and discussion

4.3.1 Effect of Reynolds number, particle size, and groove geometry

To determine the effect of Reynolds number, the distribution of 7 μm particles in the staggered herringbone mixer were analyzed at 3 different Reynolds numbers by varying flow rate. Channel Reynolds numbers of 0.02, 0.2, and 2 were accomplished with flow rates of 0.6 μL/min, 6 μL/min, and 60 μL/min, respectively. Comparing the SHM mixing 7 μm beads at Re=0.2 and Re=2 (Figure 4-2 a,b), the cross-sectional distributions of particles are very similar in all the mixing cycles. The distribution of Re=0.02 is also the same. This finding allowed the conclusion that the effect of Reynolds number in this range was minimal and the remaining experiments to be performed at a single Reynolds number.

The distributions of 7 μm particles in 3 different types of the SGM (standard, taller grooves and wider grooves) were also analyzed at channel Reynolds number 0.2 (flow rate 0.6 μL/min). The SGM with taller grooves has 50μm tall grooves instead of the 20μm tall grooves in the standard SGM. The spacing of grooves is the same as the

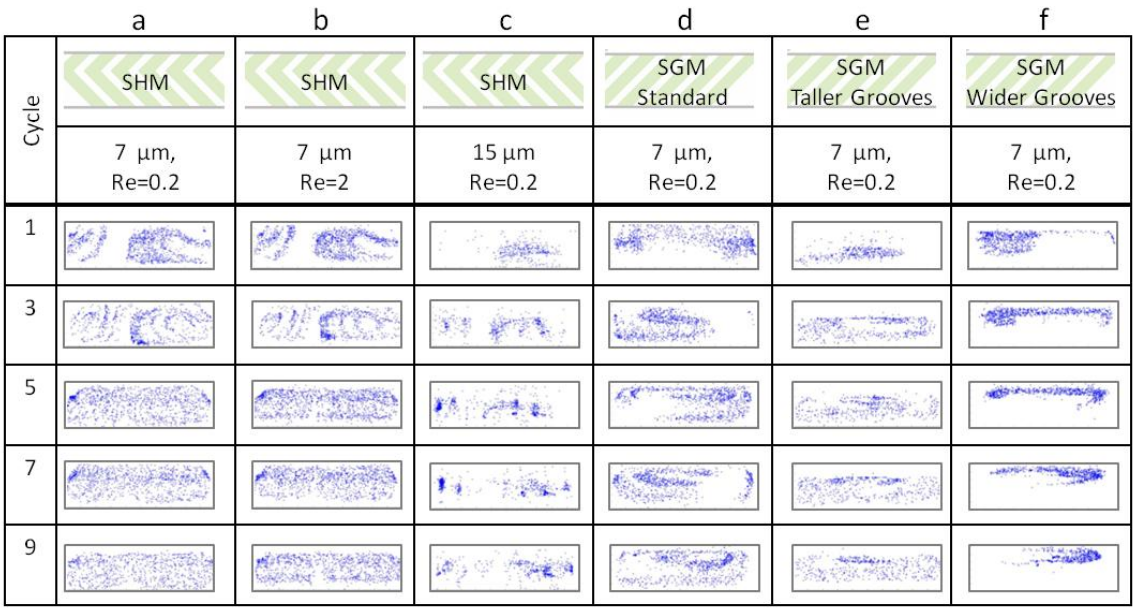

Figure 4-2. Flow rate, particle size, and groove geometry effect on distribution. Reynolds number (or flow rate) does not have a large effect on distribution when compared to the effect of particle size and geometry. Scatter plots show the distribution of florescent microparticles in the channel cross-section (*y*-*z* plane) at different experimental conditions (a-f) after 1, 3, 5, 7 and 9 cycles of grooved channel. In all cases microparticles were pumped into the right inlet while a carrier fluid (of the same viscosity, density and refractive index) was pumped in the left inlet. Therefore particles start evenly distributed on the right side of the cross-section. e) The SGM with taller grooves has 50µm tall grooves instead of the 20µm tall grooves in the standard SGM. The spacing of grooves is the same as the standard SGM. f) The SGM with wider grooves has 100µm wide grooves instead of the 50µm wide grooves in the standard SGM. These grooves are also spaced 100µm.

standard SGM. The SGM with wider grooves has 100µm wide grooves instead of the 50µm wide grooves in the standard SGM. These grooves are also spaced 100µm. Figure 4-2 d-f show the effect of groove size the particle distributions. For 7 µm beads, taller grooves appear to mix better while wider grooves appear to constrict the beads to the center of the channel. The SGM with the taller grooves has particles relatively evenly spread across the channel cross-section while the SGM with wider grooves shows a high concentration of particles at the middle with areas of no particles at the edges.

Finally, the distribution of 15 μm particles in the SHM was also analyzed at channel Reynolds number 0.2 (flow rate 0.6 μL/min). One sees specific regions of high concentration and areas with no particles at all. Compared to the mixing of 7 μm beads in the same geometry, this suggests that the mixing is much more efficient for the 7 μm beads than the 15 μm beads. More experiments to determine the effect of particle size

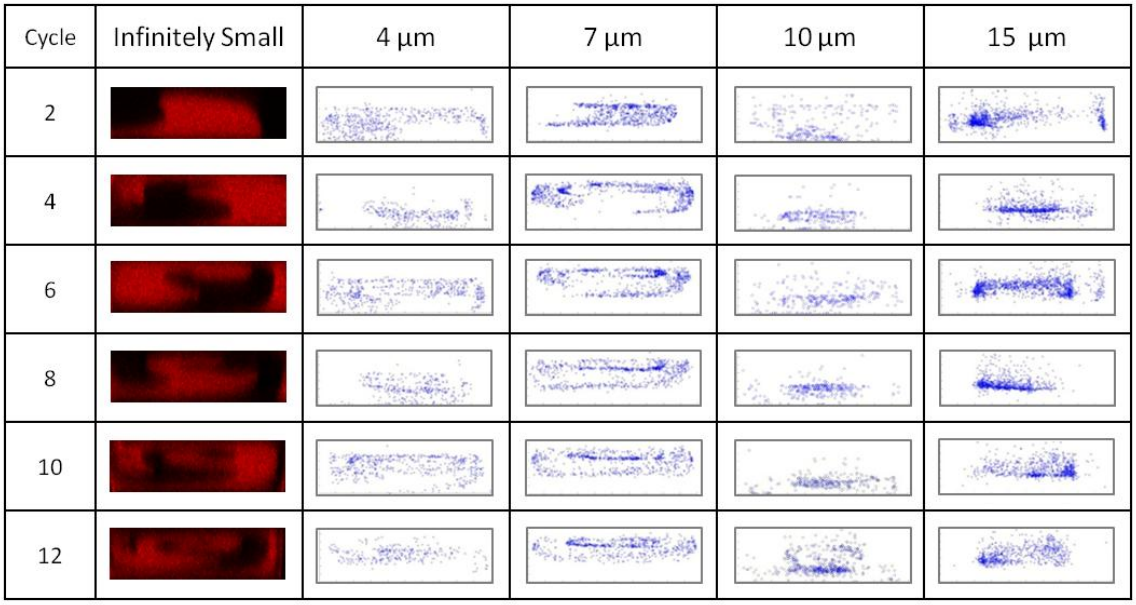

Figure 4-3. Size effects on distribution; smaller particles behave more like the fluid. All experiments are done in the standard SGM at Re=0.2. The first column shows distribution of a fluorescent solvent in the channel cross-section (y,z plane) at 2, 4, 6, 8, 10 and 12 cycles of grooved channel from confocal microscopy. Scatter plots show the distribution of florescent microparticles in the channel cross-section (y,z plane) at a different experimental conditions after 2, 4, 6, 8, 10 and 12 cycles of grooved channel. In all cases microparticles were pumped into the right inlet while a carrier fluid (of the same viscosity, density and refractive index) was pumped in the left inlet. Therefore particles start evenly distributed on the right side of the cross-section.

are shown in Figure 4-3 in the SGM at Reynolds number of 0.2, it is apparent that smaller particles behave more like the fluid. The first column of Figure 4-3 shows the distributions of fluorescent small molecule Rhodamine B, defined here as an infinitely small particle. The small molecule acts as a fluid tracer. The next 4 columns show the

distributions for 4, 7, 10, and 15 μm particles. The 4 μm beads closely mimic the flow of the fluid, closely overlapping with the dark (non red) sections of the Rhodamine distribution throughout the evolution of the cycles. As the particle size increases, the similarity to the Rhodamine distribution disappears and the mixing becomes less efficient. This supports the idea that small, point particles can be used as fluid tracers, but larger particles do not follow the fluid streamlines.

For biological applications, like in the device for T cell stimulation [36], handling and processing of cells, not beads, is necessary. It is important verify that the bead experiments are a valid model to describe the distributions of cell suspensions. Therefore, the distributions of the T cell lymphocyte Jurkat cells, labeled with calcein, were determined and compared to that of the beads in a subset of experimental conditions. Figure 4-4a shows the particle distribution concentration plots for the standard SGM and the SGM with taller grooves with 10 and 15 μm beads and Jurkat cells. The cell cross-sectional distribution is similar to that of 10 μm beads. They overlap in some areas (yellow in the image) and occupy the same general space in the channel cross-section. Similar, but not exactly the same, profiles are to be expected given that the average size of Jurkat cells (12 μm) is close to the size of the bead. Therefore, the cells distribute as would be expected based on their size and the bead experiments. This verifies that, while cells are not the same deformability as rigid beads, bead experiments are a valid model to describe distributions of cell suspensions.

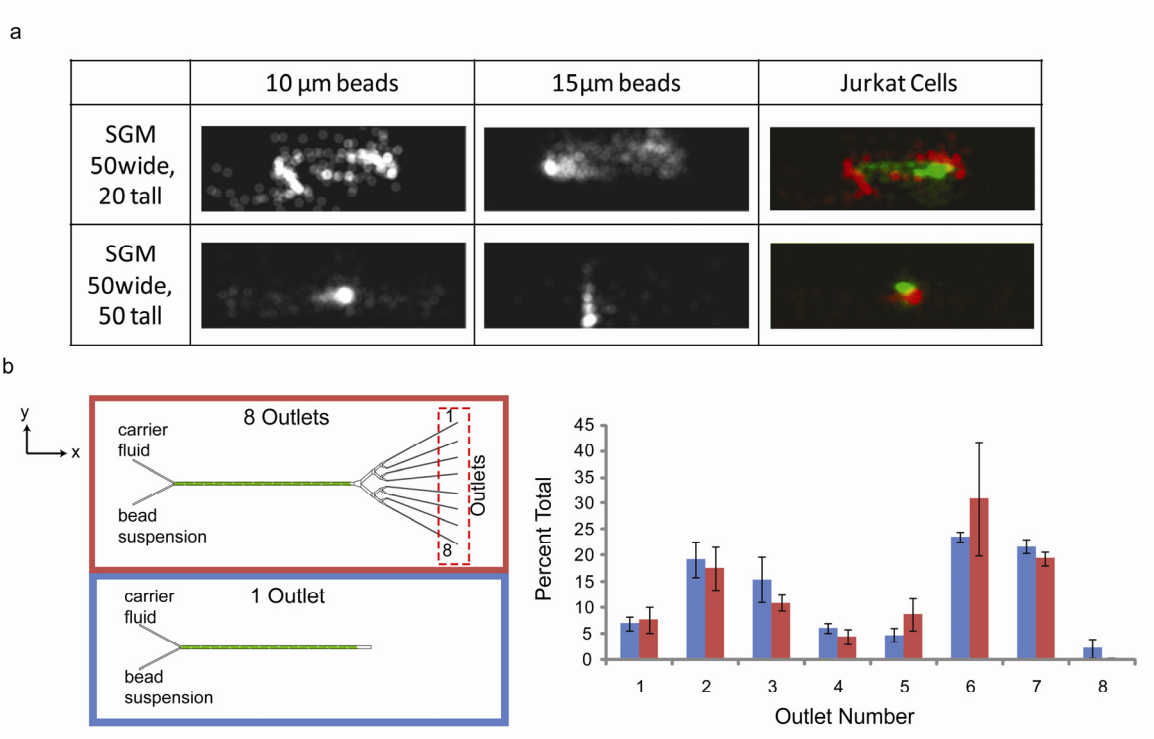

Figure 4-4. Validity of single outlet bead experiments. a) Jurkat cells distribute similar to 10 and 15 µm beads. The top row shows the concentration plots for the cross-sectional distribution after 12 cycles in the standard SGM. The bottom row shows that for a SGM with taller grooves, 50µm tall grooves instead of the 20µm tall grooves in the standard SGM. The first 2 columns represent 2 different bead sizes (10µm and 15µm) while the last column shows the data for Jurkat cells (green) overlaid on the 10 µm bead image (red). All experiments shown are at Re=0.2. b) The downstream flow splitting has no significant effect on the particle distribution. The bar graph shows the distribution in the y direction as a percent of the total particles observed. The y positions are binned into 25 µm sections to recreate the distribution from the 8 outlets. Error bar represent standard deviation, n=3.

4.3.2 Effect of downstream flow profiles

While for these experiments there was only one outlet, many applications will require splitting of the flow into multiple streams. For example, in the T cell stimulation devices from Chapter 2, the flow was split into 8 equal streams for parallel processing. Therefore it was necessary to determine what, if any, the effect of downstream splitting

has on the distribution profiles. Figure 4-4b shows the 2 different device types used in the experiment: one with one outlet and one with 8 outlets. Both devices were imaged after the 9th cycle before the outlet or splitting structure. The *y* positions were binned into 25 μm sections to recreate the distribution that would result from the 8 outlets. The plot shows similar distributions with no statistical difference and implies that the downstream flow splitting has no significant effect on the particle distribution. The downstream flow splitting does not change the particle distribution after 9 cycles.

4.3.3 Using grooved devices as a sample concentrator

As observed earlier in section groove geometry has a significant effect on particle distributions, the taller SGM results in drastically different particle distributions across the size spectrum. It mixes smaller particles slightly better (in the *y* direction) and acts as a sample concentrator for larger particles and cells. Figure 4-5a shows this phenomenon, where the 4 micron particles nearly evenly distributed across the channel in the *y*-direction of the concentration plots, and an area of high concentration in the middle for the 10 micron and 15 micron beads and Jurkat cells. This phenomenon can be taken advantage of to create a size based enrichment device or sample concentrator. Size base enrichment is important because cells are typically found in heterogeneous mixtures. For example blood is a complex mixture of many different cell types. Flow cytometry is a powerful and established tool for cell separation [77]. However, this macroscale equipment typically requires large sample volumes with negates small sample requirement and cost reduction allowed by microfluidic systems. Many microfluidic platforms exist for physical manipulation of particles using dielectrophoretic, magnetic,

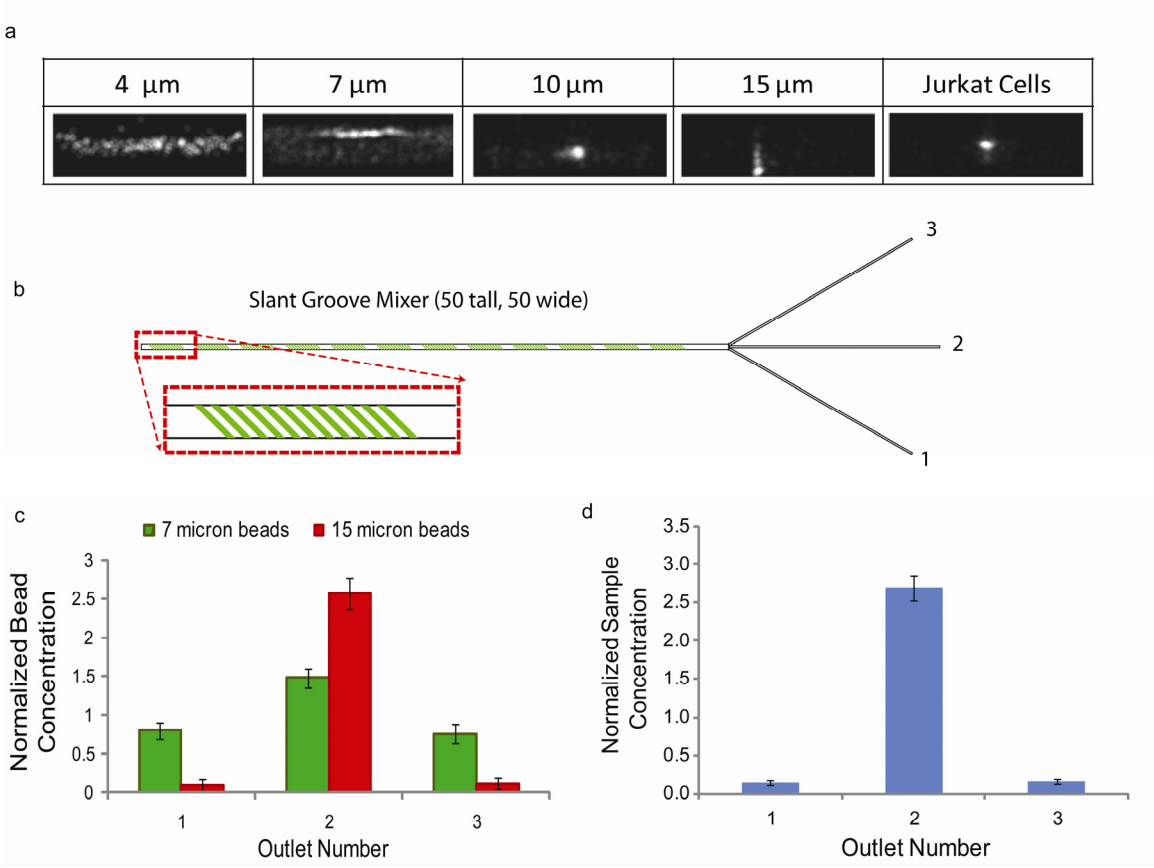

Figure 4-5. Particle concentration enrichment device. Changing from the standard SGM geometry to one with taller grooves makes a sample concentrator instead of mixer for larger beads and cells. This can be used to both enrich based on particle size (c) or as a cell sample concentrator (d). a) The concentration plot cross-sectional distributions for beads of different sizes and cells after 12 cycles in the SGM with taller grooves, 50µm tall grooves instead of the 20µm tall grooves in the standard SGM. b) Shows the enrichment/concentrator device. The beads (or cells) enter the device evenly distributed and 3 sections are taken off the end. c) The normalized concentration of beads across the 3 outlets. d) The normalized concentration of cells across the 3 outlets. In (c) and (d) the concentration is normalized to the initial inlet concentration. Error bar represent standard deviation, n=3.

optical, and acoustic fields [78-84]. All of these techniques require outside force for particle manipulation and are therefore not ideal for continuous flow applications. Hydrophoretic filtration and size based lateral displacement using microfluidic obstacles is a continuous flow alternative for size based separation [62, 85, 86] . While these devices have been show useful in many instances, clogging may be an issue around the

PDMS obstacles. Also, inertial forces were used to as a high-throughput method separate cells based on size [87, 88] . The flow rates necessary for these high Reynolds number inertial effects are incompatible with many downstream applications. This slant groove mixer, in contrast, can provide an additional low Reynolds number clog-resistant and label-free method for size based sample enrichment.

Even if a homogeneous cell population is available, i.e. no separation is necessary, for some applications a more concentrated sample than available may be needed. More directly related to the application of cell stimulation dynamics, often in cell processing, multiple steps must be performed. Several mixing and washing steps may need to be performed in series in certain applications, thus diluting the cell sample. On the macro scale, centrifugation is used to return the cells suspension to a more concentrated state after the inevitable dilution that occurs when adding stimulus solution or washing buffer. On the micro scale, we can accomplish this same reconstitution step with this unique SGM.

To prove this concept, additional devices were fabricated (shown in Figure 4-5b) with one inlet for an even initial distribution and 3 outlets for flow fractionation. The channel was made up of 12 cycles of the SGM with taller grooves. For a proof of concepts of size based enrichment, a suspension of 7 μm and 15 μm (in this case the 15 μm beads were red fluorescent, Invirtrogen) was pumped into the inlet. The starting concentration of each bead was approximately 0.25 million/mL. At the outlets, 3 samples were collected and beads counted. The resulting outlet concentrations normalized to the inlet concentration are shown in Figure 4-5c. Almost all of the 15 micron beads were in the middle outlets, while the 7 micron beads distributed between all three. This is

consistent with the imaging based results in Figure 4-5a. To demonstrate concentrating cells from suspension, a 0.5 million/mL suspension of Jurkat cells was pumped into the inlets. At the outlet, 3 samples were collected and counted. The resulting outlet concentrations normalized to the inlet concentration are shown in Figure 4-5d. Almost all of the cells are collected in the center outlet resulting in an almost 3 times the initial concentration. These two examples demonstrate that both size based enrichment and sample concentration are feasible with this design. Here we demonstrated at 3-fold increase in concentration, using 3 outlets at the same flow rate. For specific application, the outlet structure can be design such that only the section containing particles is removed from the center and the rest is sent to waste. The taller SGM confines the 15 μm beads to within a 20 μm section in the middle of the channel. Therefore, if just this section was fractioned from the rest, a 10x concentration would be possible. The area of confinement increases with decreasing bead size, to approximately 40 μm. In this case, only 50 % of the beads are confined in this space. Therefore, the best possible enrichment would be approximately 2.5x. For the application of separating the two types of beads, if necessary, one can iterate to get better separation.

Frances Ligler's group was able to create a similar 2-dimensional focusing of fluids to the center of the channel for microfluidic flow cytometry using grooved channels [89, 90]. Their method, however, required 1-dimensional focusing to the center of the channel in the *y*-direction using sheath flow. The grooves merely focused the stream away from the top and bottom walls. For large particles, the device presented in this thesis requires no pre-focusing steps.

4.3.4 Quantifying the extent of mixing

To quantitatively evaluate the effectiveness of the mixer or sample concentrator, quantification is needed. Here we used Shannon entropy to quantify the degree of mixing [91, 92]. Shannon entropy (S) depends on discretized probability distribution (p_i) across the system,

$$S = -\sum_{i=1}^{N} p_i \ln p_i$$

where the total number of bins is equal to N. If the probability in one discrete element is equal to one and zero in all others, Shannon entropy would equal 0 would, i.e. zero mixing. The largest value of Shannon entropy is achieved when the probabilities in all discrete elements are equal, i.e. perfect mixing. The exact value is dependent on the total number of discrete elements.

Mixing can be quantified in both 2-D and 1-D using Shannon Entropy. Figure 4-6 shows mixing quantification for 7 μm beads in the SHM at Re=2. In Figure 4-6b, the full cross-section is divided into 5 μm micron square sections, resulting in 546 total discrete elements. Shannon entropy is calculated and plotted for each cycle. Also, plotted is the Shannon entropy of perfect mixing with 546 total discrete elements (dashed line). As the cycle number increases, the Shannon entropy increases, but levels out at ~0.9, never reaching the perfect mixing mark of 1 (all values are normalized to the maximum possible Shannon entropy such that perfect mixing would have a value of 1). This makes sense when observing the areas void of particles in the later cycles of Figure 4-6a. However, if one is interested in the practical applications of our mixer, the mixing across the *y* direction is most important. Figure 4-6c shows the Shannon entropy for each

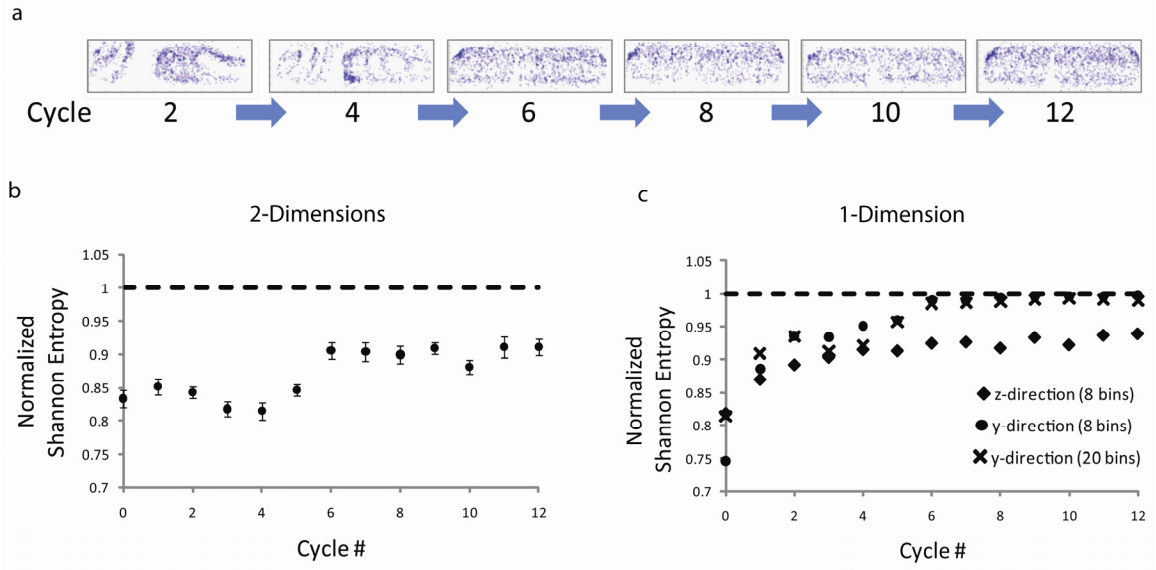

Figure 4-6. Mixing quantification. Mixing can be quantified using Shannon Entropy in both 2-D and 1-D. a) The cycle by cycle progression of mixing in SGM of 7 µm beads at Re=2 shown as scatter plots of cross-sectional distribution. b) Shows the progression of Shannon Entropy as a function of cycle number. With the bin size of 5 µm (25 μm^2), the total number of bins is 546. This gives a maximum S of 1.2, shown as the dashed line. c) Shows the progression of Shannon Entropy as a function of cycle number in 1-D for 8 bins across the channel cross-section in the y direction (consistent with the 8 outlets in the original experiment), 8 bins across the z-direction and 20 bins across the y-direction. The 1-D distribution in y-direction is practically useful for evaluating the best mixer or sample concentrator.

cycle where 1-dimensional discrete elements were used. For 8 discrete elements in the y-direction (consistent with the 8 outlets in the original experiment discussed in Chapter 2) entropy increased with increasing cycle number and levels out at 0.99. However for 8 discrete elements in the z-direction, the entropy levels out short of perfect mixing at 0.92. This indicates that the mixing can distribute the cells in the span-wise direction but not in the z-direction. Had the practical application not been considered in the method of quantification, this mixer may have been ruled out as a successful mixer for 7 micron particles. However, it is indeed quite close to a perfect mixer for all practical applications. This can be extended to other applications where more parallel

experiments are desired. Figure 4-6 also demonstrates that even with 20 discrete elements, near perfect mixing is achieved.

4.4 Experimental summary

Experiments suggest that particle size and groove geometry have the largest effect on particle distributions. Small particles develop distributions similar to those of the fluid element tracer, while large particle distributions vary widely based on the groove geometry. For finite sized particles there exists an excluded volume of streamlines near the channel wall that the particles cannot access. Therefore many streamlines necessary for rotational flow and efficient mixing are not available to larger particles. For the application of mixing in the SHM and SGM, the 4 μm beads showed good mixing, similar to solute mixing. The mixing of the 7 μm beads, while, not perfect was acceptable for many applications, demonstrating near perfect mixing, quantified by Shannon Entropy, across the 8 experimental outlets. The larger beads, 10 μm and 15 μm, demonstrated poor mixing and had distributions markedly different from the fluid tracer. These observations support the theory that small point-like particles follow fluid streamlines and can be used as fluid tracers, while, larger particles do not follow fluid streamlines and distribute differently in the channel cross-section. Channel and geometry can be changed to design a better mixer for larger particles. For example, our data suggest that for larger beads, increasing groove depth decreases mixing efficiency while increasing and groove width improves mixing slightly.

By simply changing the groove height the mixer was converted to a size-sensitive sample concentrator. For 15 μm beads and Jurkat cells we demonstrated an almost 3

fold increase in concentration using the SGM with taller grooves. A 10 fold increase in concentration is possible by simply changing the outlet structure.

Using the hypothesis of excluded volume, this result can likely be scaled to achieve an observed distribution for particles by scaling the channel geometry accordingly. For example, the device that makes a concentrator for 15 μm particles has a channel width of 200 μm and a height of 70 μm with grooves that are 50 μm wide and 50 μm tall. To scale this device to create a concentrator for 7 μm particles one would scale all by .466 (7/15) to fabricate a concentrator with the following dimensions: a channel width of ~93 μm and a height of ~32.6 μm with grooves that are ~23.3 μm wide and ~23.3 μm tall. This is possible because the most important factors to particle distributions at these conditions are the particle size and the structure and path of the streamlines. The Re number must merely be maintained within studied range (on the order of 0.01 to 1); here we know Re does not have a major effect on the particle distribution.

4.5 Numerical model for particle distribution

Many sophisticated complicated simulation methods exist for tracking particles through fluid flow. Eulerian and Lagrangian approaches are used to simultaneously solve for fluid and particle flow profiles [93, 94]. Molecular dynamics based approach evaluate particle interactions in a given fluid field [95]. At zero Reynolds number, Stokian dynamics was used to simulate pressure driven flow of particle suspensions [96, 97]. Finally, methods based in lubrication theory allow simulation of particle suspensions in a predefined fluid flow profile [98, 99]. While all these methods were

shown to predict experimental results under the similar flow condition, these simulations are extremely computationally intensive. A simpler model would be advantageous to rapidly evaluate multiple particle size and groove geometry combinations to develop the ideal mixer or sample concentrator under the given experimental conditions.

It was noted previously that particle size and groove geometry play the largest role in determining particle positions. Another way of stating this is that the most important factors are the particle size and the structure and path of the streamlines. Because of the finite size of the particles, there exist positions within the micro channel that these particles cannot occupy (within their radius, r_p, to the wall). The streamlines that flow through those positions are inaccessible to the particles at this position. Particles in these streamlines are forced to occupy another away from the wall. A simple model based on this assumption does not take into account the forces on the particle surface but is a useful approximation when the Reynolds number is small such that inertial forces are negligible and the lubrication layer is thin compared to the particle radius. To test the hypothesis that this is a major contributor to the observe particle migration pattern, we built a model assuming that when not in close proximity to the wall the particle will follow the streamline positioned at its center of mass.

4.5.1 Modeling method overview

Here we developed a model that uses streamlines generated by the commercial CFD software FLUENT® and determines particle distributions after flowing through the grooved channel. The model is based on the principle of streamline accessibility that the particles have a finite size and cannot occupy the space within its radius to the wall. The channel is cut down to the minimal repeating unit. The boundary conditions were

assigned as 4 kPa at the inlet and zero pressure at the outlet. This pressure drop approximates a 6 µL/min flow rate in the channel section (consistent with the Re = 0.2 experiments). A non-slip condition was applied to all remaining exterior boundaries. The mesh consisted of ~4.2 million elements. Velocity profiles found in FLUENT® are loaded in to Techplot®. Techplot® is used to generate streamlines (spaced 0.5 µm). Then the streamlines are loaded into MATLAB®. Each point on each streamline is evaluated for is distance to the channel walls and the streamlines are tagged for whether or not they come within r_p to the wall. If the streamline remain far enough from the wall through the whole segment, a particle starting in that streamline tracked to the end of that streamline; if the streamline comes within r_p to the wall, the particle in that streamline is pushed, normal to the wall, to a neighboring streamline and tracked accordingly.

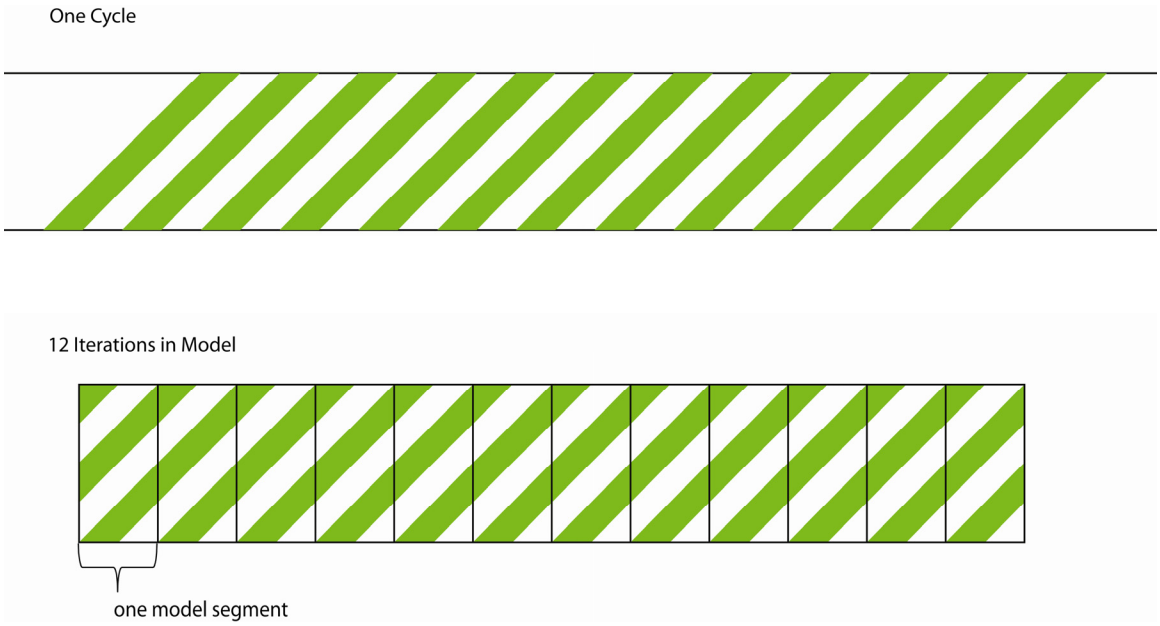

Figure 4-7. The model approximation of 1 cycle of SGM standard size. On the top, one cycle containing 12 complete grooves is show. The bottom shows how 12 model segment combines to approximate one cycle.

This process is iterated to complete 12 cycles of mixing. The minimal repeating unit is a 100 μm long section of the channel, overlapping pieces of 3 grooves. Putting together 12 times this model approximates 12 cycles (Figure 4-7). The section of the channel that the model iterates over does not completely mimic the experimental conditions - the 12 iterations result in a cycle that begins and ends with incomplete grooves. For completeness, two additional model sections, end caps, would result in a better approximation of experimental conditions. This simpler setup, however, is an acceptable starting point to prove the model hypothesis.

4.5.2 MATLAB model specifics

The streamlines are loaded as one long matrix of *x, y, z* points. *M* is an *m* x *n* matrix where *m* is the total number of points and *n* is 3 (one column for each *x, y*, and *z*). Then the next step was to label the data with the specific streamline and wall proximity information. Three more columns were created in *M* (now *n* is equal to 6). Column 4 was used to indicate the streamline number, column 5 was the point in particular streamline, and column 6 was used to identify whether that point comes with in r_p of a wall and which wall. The value in column 6 was zero if the point was far enough from the wall; else the number in the column represents which wall the point was close to. This number was used later to determine which direction to move the particle. Simultaneously 3 new matrices were created. *MM* was a higher order version of *M* where each streamline was in its own matrix; *MM* was an *m* by *n* by *p* matrix where *m* was the length of the streamline, the six columns represented the same as that in *M*, and *p* is the total number of streamlines. Also, a matrix of the first points of each streamline was created (*Init*). *Init* was a *p* by 5 matrix. Where the first three columns gave *x, y, z* coordinates. The 4th

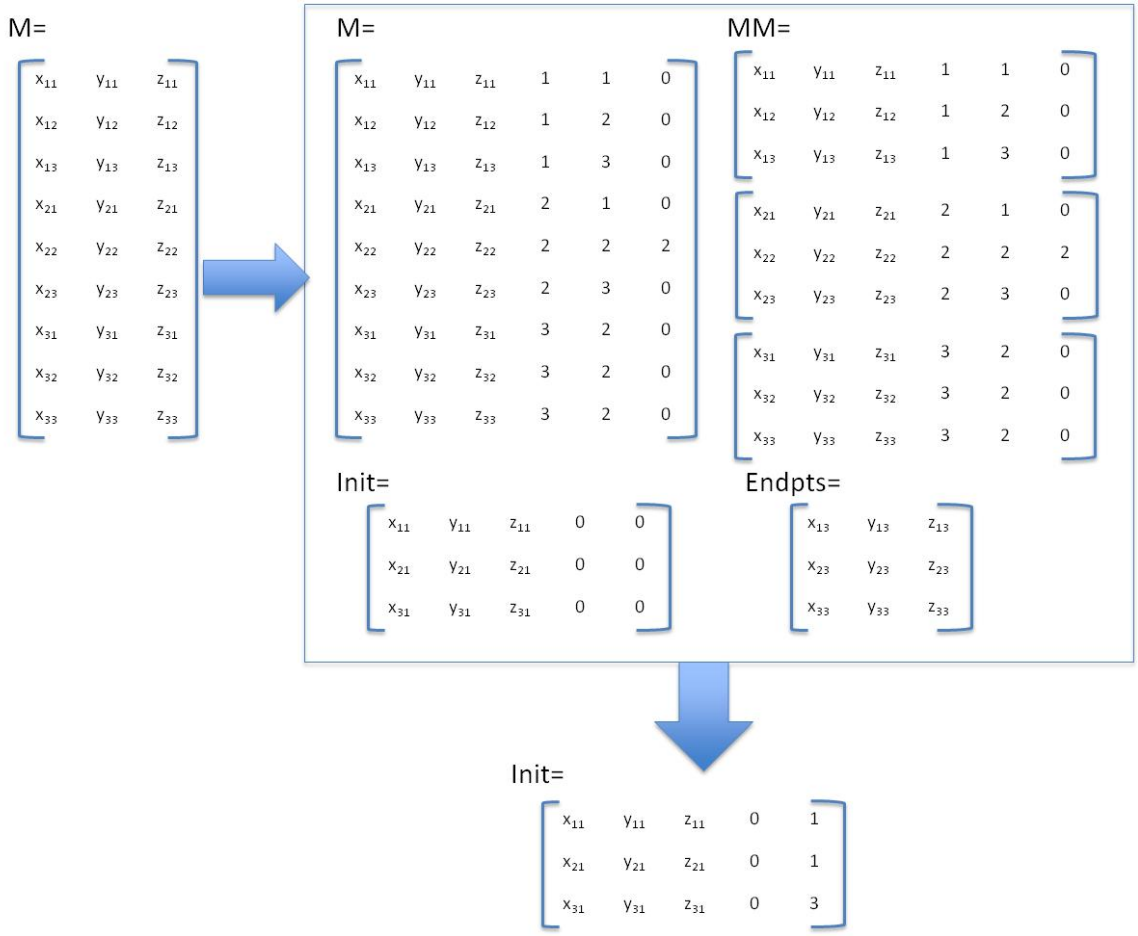

Figure 4-8. The structure and formation of the matrices used in the numerical model. First *M* is a long matrix of streamlines listed end to end. Then the matrix *M* was labeled with streamline specifics and wall proximity information. The 2 indicates that point came within the particle radius of the wall at y = 200 μm for example. Simultaneously the a matrix for each streamline (*MM*), a matrix of initial points (*Init*) and a matrix of final points (*endpts*) was created. Finally, *Init* is labeled with the index of its endpoint in *endpts*; the same as its initial index if it does not come close to the wall.

column indicated whether or not that point was further than r_p from the wall. If it was in an accessible position the value was 1 if not the value is 0. And the 5th column was used to designate the streamline a particle would end up in after one iteration through the minimal repeating unit; at first this column was filled with zeros. Finally a matrix of the last points of each streamline was created (*endpts*). The variable *endpt*s was a p by 3 matrix of the x, y, z coordinates. The row indices of *Init* and *endpts* matched such that

the rows of each represented the first and last points of the same streamlines, respectively.

After all the needed matrices were created, the 5th column of *Init* was label with its corresponding final particle position (this is different from the fluid element final position in *endpts* for some streamlines that come too close to the wall). For all the streamlines, the 5th column of the corresponding *MM* matrix was checked to see if it contained any values that represented wall hits. If the column was all zeros, there was no wall contact and the 5th column of *Init* was labeled with its own indices, i.e. it ends up in the same streamline it starts. If the particle came too close to a wall the 5th column of *Init* would contain a number corresponding to which wall. The particle was then moved to the next streamline normal to that wall. If that streamline stayed clear of the wall, it would continue to the end; if not the process would repeat until the end was reached. The 5th column of *Init* would be labeled with the indices corresponding to the streamline the particle was in when it reached the end of the minimal repeating unit. This process was continued for each row of *Init* until it was completely labeled such that each starting point had a matching ending point in the *endpts* matrix; the number in column 5 of *Init* gave the indices of the point in *endpts*.

The last step before iterations could be performed was mapping the points in *endpts* back onto the original grid of the *Init* points. The points in *Init* were evenly spaced every μm on a grid and, while the spacing *endpts* is still close to a μm, the *endpt* points do not exist on the same grid. Therefore a partial least squares method was used to find the closest 4 points on the original grid and the distances from each of those points. The endpoint was then mapped onto the initial grid by weighting the distance from it to

all 4 points. In the example in Figure 4-9a, the distance between the endpoint and its 4 closest starting points (d_i) was 0.25 microns, 0.35 microns, 0.25 microns and 0.4 microns for initial points 1, 2, 3 and 4, respectively. The closer the points are, the higher the weight. This determined by the formula

$$Weight_i = \frac{1/d_i}{\Sigma\left(1/d_i\right)}$$

This weighting system was used to maintain continuity when iterating over a discrete set of streamlines. This process with example numbers is shown for one endpoint in Figure 4-9b. In this case, 30 % of the value in the endpoint was mapped onto Init point 1, 21% onto Init point 2, 30% onto *Init* point3, and 19% onto *Init* point 4. This process of splitting the particle up into discrete streamlines likely introduces some error, but is a good approximation of the probability of the particle in any of the given streamlines.

Once the particle paths across the minimal repeating unit were complete mapped out, iteration was possible where in the ending position became the next starting position, for the next segment of the mixer. A final accumulative matrix is created called *Values*. The first 2 columns represented the *y* and *z* position of the particles (same grid as those in *Init*). Then each subsequent column contained a value representing how many particles existed in that streamline for each iteration, starting with zero on the left side ($y < 100$ μm) and 1 on the right side ($y > 100$ μm) before mixing. The grid in Figure 4-9b shows this mapped out with values in each streamline shown at each grid point (*y,z* coordinate) for Cycle 0 (before mixing) and a hypothetical situation after 1 cycle. The minimal

a

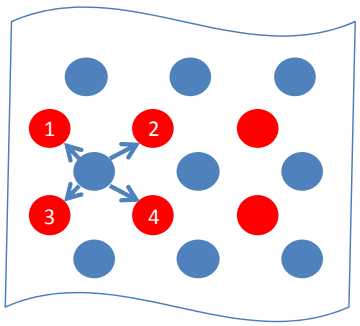

Distances and weights from Endpt to 4 closest Init points

d1=0.25 → w1=0.30
d2=0.35 → w2=0.21
d3=0.25 → w3=0.30
d4=0.4 → w4=0.19

b

Cycle 0

0	0	0	0	0	0	0	0	0	0	0	0	0	0	0	0	0	0	0
0	0	0	0	0	0	0	0	0	0	1	1	1	1	1	1	1	1	0
0	0	0	0	0	0	0	0	0	0	1	1	1	1	1	1	1	1	0
0	0	0	0	0	0	0	0	0	0	1	1	1	1	1	1	1	1	0
0	0	0	0	0	0	0	0	0	0	1	1	1	1	1	1	1	1	0
0	0	0	0	0	0	0	0	0	0	1	1	1	1	1	1	1	1	0
0	0	0	0	0	0	0	0	0	0	0	0	0	0	0	0	0	0	0

Cycle 1
(6 iterations)

0	0	0	0	0	0	0.25	0	0	0	0.25	0.25	0	0.25	0.25	0.25	0.25	0	0	0
0	0	0	0	0.25	0.5	0.5	1	0.5	0.5	0.5	0.5	0.5	1	1	1	1	0.5	0.5	0
0	0	0	0	0.25	0.5	0.5	1	0.5	0	1	0.5	1	1	1	1	1	1	1	0.25
0	0	0	0	0	0.25	0.25	0.5	0	0	1	1	1	1	1	1	1	1	1	0.25
0	0	0	0	0	0	0	0	0	0	0.5	1	0.5	0.75	0.75	0.75	1	1	1.25	0.25
0	0	0	0	0	0	0	0	0	0	0.25	0	0	0	0	0	0.75	1.25	1.75	0
0	0	0	0	0	0	0	0	0	0	0	0	0	0	0	0	0	0	0	0

Figure 4-9. Mapping of particle positions. a) Remapping of particle exit positions (blue, *endpts*) onto entry positions (red, *Init*). b) Values at particle positions before and after 1 cycle of mixing.

repeating unit was iterated through 12 times to model flow through one cycle. Finally the coordinates and values were used to generate concentration maps that could be compared to experimental results for each cycle (like shown in Figure 4-10).

This code can be easily adapted to changing particle size and does not need to be completely re-run. All matrices are be stored, such that in changing the particle size, the model only needs to be run from the point of labeling *Init* with its end position. However, a new geometry requires starting with a new FLUENT® model.

4.5.3 Model comparison to experiment

This model was used to track 7 micron particles through the standard SGM and determine the resulting distributions after each cycle. These distributions were compared to the result of experiments in Figure 4-10. The model captures some of the major features and qualitatively predicts the experimental distributions; the concentration plots of cross-sectional distributions for the experiment and model roughly match with a few

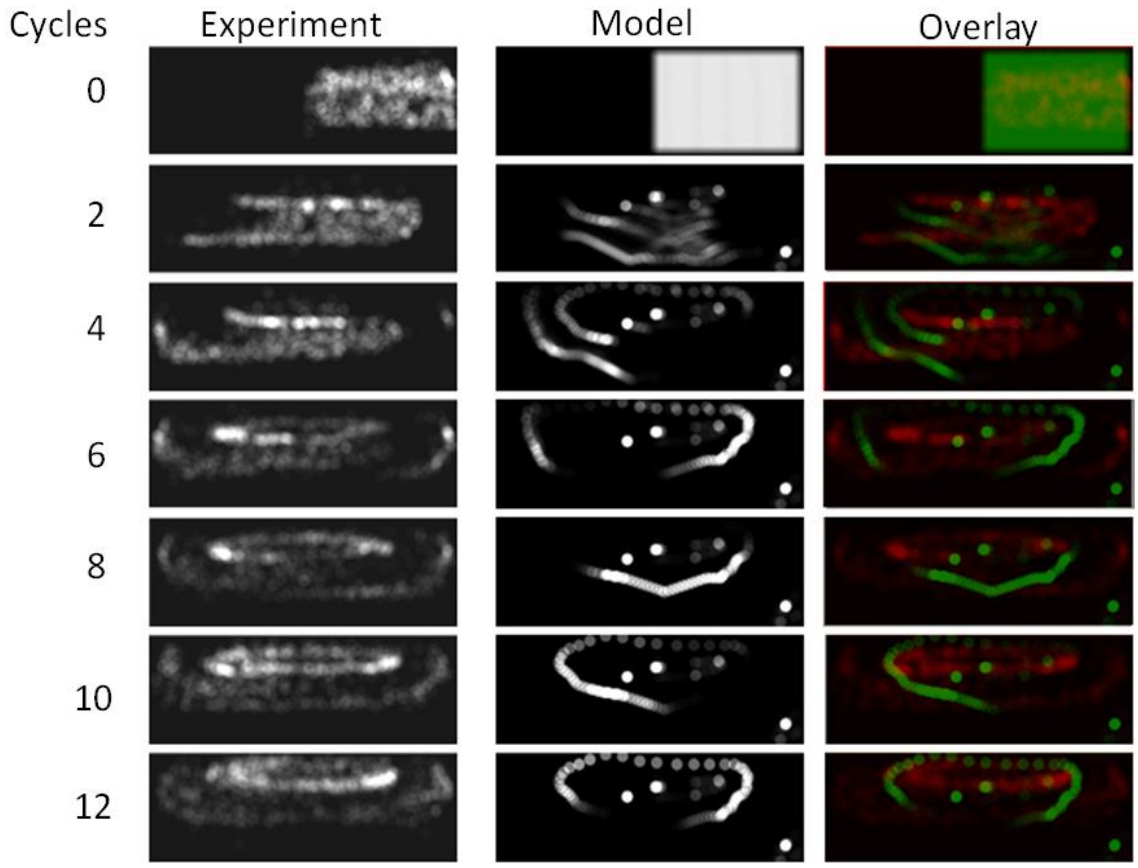

Figure 4-10. Model comparison to experiment. The model roughly mimics the distribution from the grooved mixer. The model (middle column) is compared with the experimental data (left column) for each of the mixing cycles. Both sets of data are shown as concentration plots of the cross-section (y,z plane) and overlaid (experiment=red, model=green) in the (right column).

exceptions. In general, the particles in the experiment are further from the walls in the z direction and are more spread in the y-direction. Also, in the bottom right corner of the model concentration map, a bright spot appears and persists throughout all iterations. The streamline that ends at this (y,z)-coordinate started at approximate the same (y,z)-coordinates. Therefore when a particle enters this set of streamlines, it never leaves. One possible explanations for why this phenomenon is present in the model and not in the experiments is that the streamline mesh is discrete and not fine enough to capture the subtle (y,z) displacements over the short iteration distance, especially because remapping of exit positions to inlet positions is required. A finer grid of streamlines or a longer iteration distance would reduce this error with added computational cost. Additionally, the experiment is a time average while the model is a deterministic endpoint. The probability density of the model could be quite different if the velocity was used to take the time average, but the final accessible positions would remain the same.

While subtle differences between the experiment and model do exist, the fact that the model captures the general trend suggests that the assumption that the experimental observations are a result of inaccessible streamlines is valid. With increased streamline density and a longer iteration distance, the model will be a useful tool to track predict particle distributions and inform design of efficient unit operations on cells and particles in microfluidic devices.

4.6 Summary

The simple model used streamlines generated by the fluid velocity profile, solved using commercial CFD software, to track finite sized particles through complex 3-

dimensional flow geometries. A model based on the assumption that particles experimental particle distributions were a result of finite sized particles being excluded from streamlines close to the wall was used to track particles through the grooved channel. This model captured the general trends in the distribution and therefore verified that the principle of accessible streamline is governing under these flow conditions. With a finer streamline grid, this model could be used to track particles through varying combinations of groove geometries to identify the best mixer.

CHAPTER 5

CONCLUSIONS AND RECOMMENDATIONS FOR WORK

5.1 Thesis contributions

This work contributed to the development of microfluidic platforms as powerful tools for probing areas of biology and medicine that were difficult with existing technology, specifically with increased speed and efficiency of data generation. This high-throughput format enabled simple and fast generation of large sets of quantitative data, with consistent sample handling. The main research objective was to design a microfluidic device for cellular stimulation that will 1) minimize stress on the cells, 2) provide reproducible results from experiment to experiment, 3) produce quantitative results comparable to or better than bench-top schemes, 4) be scalable to high throughput formats, 5) minimize consumption of cells and reagents, and 6) provide the temporal resolution that the bench-top counterparts cannot achieve. All of these were accomplished in some way: 1) The multi-time point stimulation devices using the Staggered Herringbone mixer exhibited stress protein levels within the normal range; 2) Experiment to experiment variation in the microfluidic device was far less than that of conventional benchtop experiments. 3) Quantitative results data from the device more closely fit the dynamics expected from the TCR pathway. 4) Our device is capable of performing 8 experiments in parallel. 5) The device used only 10% of the reagents necessary in conventional benchtop methods. 6) Finally, rapid mixing provided exceptional temporal resolution especially when compared to that possible by hand.

5.1.1 Parallel multi–time point cell stimulation

In the context of early time point T Cell signaling dynamics, our device successfully accomplished a multi-time point stimulation experiment with on-chip cell lysis. Rapid mixing, achieved with the staggered herringbone array, allowed precise time point resolution down to 20 seconds. Modeling and confocal mixing experiments gave valuable insight into the mixing of solutions, with a wide range of fluidic properties, relevant to biological experiments. The flexible nature of this modular design allowed easy adjustment of time points without changing the device or operation conditions. This one-time-use device was inexpensive to fabricate, simple to set up, and simple to use. The flexibility and potential for automation in the microfluidic format allows for future development for more "online" processing of samples, which may further reduce necessary sample volumes and cell concentrations. From a single experiment, 6 proteins were analyzed simultaneously for 8 time points, yielding 48 measurements from only 10 million cells, only 5% of the amount needed in conventional methods [11]. The ease of use and applicability of this device was demonstrated through use by biologist and other non micro fluidic experts across GA Tech's campus. Other labs, with less micro fluidic experience, will benefit from the ease in set up and negligible human interaction necessary after initial set up. One merely must plug in the tubings, fill and hook up the syringes, and collect their sample.

5.1.2 STEP imaging for 3-D particle tracking

Additionally, we have shown in this thesis a novel STEP imaging technique that can be used to discern the details of the particle positions and distributions, and track particles in complex flows, in an inexpensive and fast manner. It is easy and practical to

implement, and only requires a conventional epifluorescence microscope. It provided single particle information faster and with more spatial information than confocal microscopy, which was the only way thus far to observe distributions of fast flowing particles in 3D. STEP imaging is also advantageous in applications where fast acquisition and processing are required to study time-dependent phenomena and where fast confocal is not available. Because the STEP imaging technique does not require additional equipment, we believe it can be easily applied by any laboratory for fast and accurate particle tracking or mapping in three dimensions. The STEP imaging technique is easily adapted to a variety of flow systems and particle sizes by simply generating a new calibration curve. Particle tracking using STEP imaging to generate three-dimensional spatial information is a necessary step towards designing the next generation mixers, separators and manipulators for a variety of application and improving their performances as particles.

5.1.3 Particle distributions in complex flow

Experimental evidence that particle size and groove geometry have the largest effect on particle distributions led to the development of a numerical model for determining particle distributions from fluid flow fields. This model was based on the assumption that particles experimental particle distributions were a result of finite sized particles being excluded from streamlines close to the wall. We believe that, with a few small adjustments, it can be used to track particles through complex flow geometries and lead to the development of the next generation of unit operations on particles in microfluidic devices.

In addition, a scheme for efficient sample enrichment was developed. By altering groove geometry, the grooved mixer was made into a sample concentrator capable of increasing particle concentration up to 10 fold.

5.2 Areas for future work

5.2.1 Adaptation of stimulation device

Other groups at GA Tech have begun to use the multi-time point stimulation device for other application in T Cell stimulation. Catherine Rivet adapted the device to include the capability of achieving lysis and fixation simultaneously [100]. Lysates provide population based measurements compatible with downstream off-chip high throughput proteomics. Fixed cells analyzed by flow cytometry reveal the existence of subpopulations and phenotypic variations within genetically identical cells. Using this device she was able to develop a multivariate model and highlights the importance of both mean values and heterogeneity in the cell population to predict the quality of T cell population. Prof. Greg Gibson's group (GT Biology) is also using an adaptation of this design to assay T cell dynamics from patient population. We expect this device to be easily adapted to many applications in cell signaling dynamics.

Additionally, we expect a high-throughput format of this device coupled with multiplexed biochemical analysis to yield large sets of quantitative data for reconstructing signaling networks in many applications. For the clinical application in T-Cell dynamics, this device must be adapted to process samples extracted from human blood. Also, pre-treatment of cell lines with siRNA or drugs may lead to more informative signal transduction studies. For these applications, additional sample

preparation may be necessary, such as selection to remove unwanted cells by size or washing steps to remove unwanted soluble signals. The development of efficient unit operations on cells and particles will aid this design.

5.2.2 Informed design of unit operation on cells and particles

With increased streamline density and a longer iteration distance, the model will be a useful tool to track predict particle distributions and inform design of efficient unit operations on cells and particles in microfluidic devices. The generation of a library of flow fields in a range of channel and groove geometries and the extraction of useful model information this can be used to for informed design of the ideal mixer or sample concentrator for a particular application. The numerical model for particle distribution contains information that can be used to create a function relating particle positions after each grooved segment to their inlet position can be created from the model. A correlation can be found for each geometry/bead size combination we try. With this information the best combination needed to achieve the desired final result (be it mixing or concentration) from a given initial distribution can be found.

APPENDIX A

MATLAB CODE FOR STEP IMAGING

```
      %% finding boundary
      % m=imread('bg1.tif');
      % m=m(10:1:end-10, 10:1:end-10);
      % imshow(m,[]);

      close all
      clc
      clear

      %before starting go through all the bg1 images using the "finding
boundary"
      %code from above and define upper and lower wall, there is an
upper
      %boundary and lower boundary for the initial and each cycle (13
total)
      upper=[204,231,259,286,261,256,295,280,333,340,231,297,318];
      lower=[636,658,682,712,691,684,721,700,757,765,657,722,739];

      counter=0;
      flowrate=[3,30] %two flowrates were done for each experiment
      for fl=1:2
          flow=flowrate(fl)

          for b=1:13 %1:# of cycles
              xy_value=[];
              z_value=[];
              a=b-1;
              for q = 1:900 % 1 : # of pictures
                  counter = q
                  %% Loading
                  %    more than 100 pix

                  if q<10
                      name =
strcat(int2str(a),'/',int2str(flow),'/series00',int2str(q),'.tif');
                  elseif q<100
                      name =
strcat(int2str(a),'/',int2str(flow),'/series0',int2str(q),'.tif');
                  else
                      name =
strcat(int2str(a),'/',int2str(flow),'/series',int2str(q),'.tif');
                  end

                  img1=imread(name);
                  bgmean=mean(mean(img1));
                  %% image modification
                  img1_1 = imadjust(img1,stretchlim(img1,
[0,0.989]),[]); %stretchlim(img1)
                  %% Gaussian Method
                  PSF = fspecial('gaussian',100,7);
```

```
                    img2 = imfilter(img1_1,PSF,'conv');
                    img2 = imfill(img2,'holes');
                    %% cutoff 10 pixel edge
                    img2 = img2(10:1:end-10, 10:1:end-10);
                    img1 = img1(10:1:end-10, 10:1:end-10);
                    [imr,imc]=size(img1);
                    %% Thresh methods
                    [thresh, EM] = graythresh(img2);
                    img3 = im2bw(img2,thresh);
                    %% Cleaning
                    img3 = bwmorph(img3,'clean');
                    img3 = bwmorph(img3,'spur');
                    img3 = bwmorph(img3,'hbreak');
                    img3 = bwmorph(img3,'majority');
                    img3 = imfill(img3,'holes');
                    %% Processing
                    % Eliminating empty image
                    bw = bwlabel(img3);
                    props = regionprops(bw,img1,'Centroid');
                    nn=length(props);
                    if nn>10 || sum(sum(img3))/(imr*imc)>0.3
                        img3=zeros(imr,imc);
                    end
                    % Start processing
                    bwl = bwlabel(img3);
                    bwprops =
regionprops(bwl,img1,'Centroid','PixelValues','BoundingBox','Solidity')
;
                    n=length(bwprops);
                    M=regionprops(bwl,img1,'MeanIntensity');
                    for i=1:1:n

                        centroid=bwprops(i).Centroid;
                        cenr=round(centroid(2));
                        cenc=round(centroid(1));
                        if bwprops(i).Solidity > 0.92 && cenc < (imc-2)
&& cenc > 2 %eliminating overlaping particles and particle too close to
the edge
                            intensity=bwprops(i).PixelValues;
                            temp=bwprops(i).BoundingBox;

                            xm=cenc;
                            yu=cenr-round(temp(4)/2);
                            yd=cenr+round(temp(4)/2);
                            ss=[];
                            ddiff=[];
                            for g=1:1:3
                                gau=[];
                                gau=(img1(yu:1:yd,xm-2+g))';
                                w=length(gau);
                                gau=gau-200;
                                gau=double(gau);
                                gau=gau(gau~=0);
                                gaux=[];
                                gaux=1:1:length(gau);
                                %% gaussian distribution
```

```
                            if length(gau)>25
                                [cfun]=fit(gaux',gau','gauss3');
                                coe = coeffvalues(cfun);
                                check=[coe(2),coe(5),coe(8)];
                                [C,I]=max(check);
                                if C>400
                                    check(I)=check(I)-check(I);
                                end
                                p1=min(check);
                                p2=max(check);
                                diff= abs(p2-p1);
                                if diff>25
                                    s=100;
                                else
                                    if length(gau)<100
                                        if gau(1)==max(gau)
                                            s=100
                                        elseif
gau(length(gau))==max(gau)
                                            s=100
                                        else
                                            [cfun] =
fit(gaux',gau','gauss1');
                                            coe = coeffvalues(cfun);
                                            s = coe(3)/(2^0.5);
%extract sigma value
                                        end
                                    else
                                        s=100;
                                    end
                                end
                            else
                                s=100;
                                diff=60;
                            end
                            if s>100 % eliminate unusual particle
                                s=100;
                            end
                            else s=100

                                s=double(s);
                                ss=[ss,s];
                                ddiff=[ddiff,diff];
                        end

s=(ss(1)^2+ss(2)^2+ss(3)^2)/(ss(1)+ss(2)+ss(3)); %taking average sigma

diff=(ddiff(1)^2+ddiff(2)^2+ddiff(3)^2)/(ddiff(1)+ddiff(2)+ddiff(3))

                        %% apply empirical curve fitting (s really is
corrected location)
                        if s<15.5
                            z_val=32.11*exp(0.02095*s)+(-498.2*exp(-
0.4534*s))
                        else
                            z_val=0.7432*(diff)+ 18.638
```

```
                        end


                        %% building matrix
                        xy_value=[xy_value, [cenr;cenc]];
                        z_value=[z_value,z_val]; %using gaussian
distribution

                    end
                end
            end

            %% define channel boundary
            top=70; %Channel height, for best quality, constrain
channel height to within 70um
            bottom=0; % always 0
            upperwall=upper(b); %channel walls %upper(b)
            lowerwall=lower(b); %lower(b)
            transport=0;
            chansize=200; %channel width

            %% rearrange data points base on channel boundary
            y_loc=xy_value(1,:);
            z_loc=z_value;
            y_result=[];
            z_result=[];
            z_loc=z_loc+transport;

            for i=1:1:length(y_loc)
                if y_loc(i)<=lowerwall && y_loc(i)>=upperwall &&
z_loc(i)<=top && z_loc(i)>=bottom
                    y_result=[y_result,y_loc(i)];
                    z_result=[z_result,z_loc(i)];
                end
            end
            y_result=round((y_result-
upperwall).*(chansize/(lowerwall-upperwall)));

            %% generate concentration mapping
            parsize=73; %pixels
            parlen=floor(parsize/2);
            par=double(par);
            samplemap=zeros(top*10+2*parsize,chansize*10+2*parsize);
            for i=1:1:length(y_result)
                pz=z_result(i)*10+parsize;
                py=y_result(i)*10+parsize;
                samplemap(pz-parlen:1:pz+parlen, py-
parlen:1:py+parlen)=samplemap(pz-parlen:1:pz+parlen, py-
parlen:1:py+parlen)+par;
            end
            map=samplemap(end-parsize:-1:parsize+1,parsize+1:1:end-
parsize);

            %this is to creat the matrix for the contour plot
            [rrr,ccc]=size(map);
```

```
                ssss=sum(sum(map));
                xxxx=ssss/(rrr*ccc);
                matrix=zeros(51200,3);
                cccounter=0;
                for ii=1:5:rrr
                    for jj=1:5:ccc
                        cccounter=cccounter+1;
                        matrix(cccounter,:)=[jj,rrr+1-
ii,map(ii,jj)/xxxx];
                    end
                end
                yzdata=[y_result',z_result'];
                pointdata=sprintf('%dulpermin/yzdata%d.xls',flow,a);
                concdata=sprintf('%dulpermin/concdata%d.xls',flow,a);
                xlswrite(pointdata,yzdata);
                xlswrite(concdata,matrix);
                mapp= uint8(map);
                mapp= imadjust(mapp,stretchlim(map, [0,1]),[]);
%stretchlim(map)
                high=max(mapp);
                high=max(high);
                %% Plotting
                imagename1=sprintf('%dulpermin/newscat%d.jpg',flow, a);
                imagename2=sprintf('%dulpermin/newconc%d.jpg',flow, a);
                figure(1); scatter(y_result, z_result,15);axis([0
chansize bottom top]);daspect([1 1 1]);
                saveas(gcf, imagename1,'jpg')
                figure(2);imshow(mapp,[0,high],'InitialMagnification',20)
                saveas(gcf, imagename2,'jpg')


            end

        end
```

APPENDIX B

MATLAB CODE FOR PARTICLE TRACKING

```
clear
clc

bead=7; %approx diameter microns of paticle
rp=3.5; %radius of particle in microns
top=90; %the height of channel plus grooves

N=[]; %N is a matrix of all the streamlines
%read all the streamlines exported from TechPlot
for i=1:20
    name=strcat('slant5020\slant5020_',int2str(i),'.xlsx');
    M=(xlsread(name))*1e6;
    N=[N;M];
end

%%clean up the matrix, take out all text and replace with zeros.

for i=1:length(N)
    if isfinite(N(i))==1
        N(i,:)=N(i,:);
    else
        N(i,:)=[0 0 0];
    end
end

%create a new matrix that N will be part of
P=zeros(length(N),6); % 4th column will be used to identify
streamlinenumber, the 5th will mark point the come to clost to the wall

P(:,1)=N(:,1);
P(:,2)=N(:,2);
P(:,3)=N(:,3);

ind=find(P(:,3));


M=[];

count=1;
lenghtstreams=length(nonzeros(N(:,2)));
M=zeros(lenghtstreams,6);
%take out all the zeros
for n=1:2:(length(N)-1)%every 2 has a 0.5 micron step size in x
    if P(n,1)<200.1
    if P(n,2)==0
    else
        M(count,:)=P(n,:);
        count=count+1;
    end
    end
```

```
      end

      lenghtstreams=length(nonzeros(M(:,2)));
      M=M(1:lenghtstreams,:);

      %start defining the matrix of inital points, the first inital
point is the
      %first row of the matrix
      init=[M(1,1),M(1,2),M(1,3)] ;
      count=1;
      streamnum=1; %start at one and count up to total number of
streams

      for n=1:(length(M)-1) % this set of if statements determines
whether or not the streamline comes close to a wall
      if M((n),1)< M((n+1),1)
              M((n),4)=streamnum; %the 4th column identifies the
streamnumber
              M(n,6)=count;
              count=count+1;
          else
              M((n),4)=streamnum; %the 4th column identifies the
streamnumber
              M(n,6)=count;
              count=1;
              streamnum=streamnum+1; %add a new stream
              init=[init;M(n+1,1),M(n+1,2),M(n+1,3)]; %add a new
initial point
          end
          if M((n),2) < rp %first y wall
              M((n),5)=1;
          elseif M((n),2) > (200-rp) %2nd y wall
              M((n),5)=2;
          elseif M((n),3) < (rp) %channel bottom
              M((n),5)=3;
          elseif M((n),3) > (70-rp) %rectangular channel top
              %% the groove geometry (width) specific part

              y=[M((n),1)+150;  M((n),1)+100  ;M((n),1)+50;  M((n),1);
M((n),1)-50;M((n),1)-100;M((n),1)-150;M((n),1)-200;M((n),1)-250];
              if M((n),1) < 50 % this set determines if it is in a
herringbone, if not then it is excluded after top-rp
                  if M((n),2)> (y(4)-rp) && M((n),2)< (y(3)+rp)
                      if M((n),2)> (y(4)) && M((n),2)< (y(3)) %this is
not in the hb
                          M((n),5)=4;
                      elseif M((n),2)> (y(4)-rp)
                          M(n,5)=6;
                      else
                          M(n,5)=5;
                      end
                  elseif M((n),2)> (y(2)-rp) && M((n),2)< (y(1)+rp)
                      if M((n),2)> (y(2)) && M((n),2)< (y(1))
                          M((n),5)=4;
                      elseif M((n),2)> (y(2)-rp)
                          M(n,5)=6;
```

```
                    else
                        M(n,5)=5;
                    end
                end
            elseif M((n),1) > 50 && M((n),1) < 100
                if M((n),2)< (y(5)+rp)
                    if M((n),2)< (y(5))
                        M((n),5)=4;
                    else
                        M(n,5)=5;
                    end
                elseif M((n),2)> (y(4)-rp) && M((n),2)< (y(3)+rp)
                    if M((n),2)> (y(4)) && M((n),2)< (y(3)) %this is
not in the hb
                        M((n),5)=4;
                    elseif M((n),2)> (y(4)-rp)
                        M(n,5)=6;
                    else
                        M(n,5)=5;
                    end
                elseif M((n),2)> (y(2)-rp) && M((n),2)< (y(1)+rp)
                    if M((n),2)> (y(2)) && M((n),2)< (y(1))
                        M((n),5)=4;
                    elseif M((n),2)> (y(2)-rp)
                        M(n,5)=6;
                    else
                        M(n,5)=5;
                    end
                end
            elseif M((n),1) > 100 && M((n),1) < 200
                if M((n),2)< (y(7)+rp) && M((n),2)> (y(8)-rp)
                    if M((n),2)< (y(7)) && M((n),2)> (y(8))
                        M(n,5)=4;
                    elseif  M((n),2)< (y(7)+rp)
                        M(n,5)=5;
                    else
                        M(n,5)=6;
                    end
                elseif M((n),2)< (y(5)+rp) && M((n),2)> (y(6)-rp)
                    if M((n),2)< (y(5)) && M((n),2)> (y(6))
                        M(n,5)=4;
                    elseif M((n),2)< (y(5)+rp)
                        M(n,5)=5;
                    else
                        M((n),5)=6;
                    end
                elseif M((n),2)> (y(4)-rp) && M((n),2)< (y(3)+rp)
                    if M((n),2)> (y(4)) && M((n),2)< (y(3)) %this is
not in the hb
                        M((n),5)=4;
                    elseif M((n),2)> (y(4)-rp)
                        M(n,5)=6;
                    else
                        M(n,5)=5;
                    end
                elseif M((n),2)> (y(2)-rp) && M((n),2)< (y(1)+rp)
                    if M((n),2)> (y(2)) && M((n),2)< (y(1))
```

```
                        M((n),5)=4;
                    elseif M((n),2)> (y(2)-rp)
                        M(n,5)=6;
                    else
                        M(n,5)=5;
                    end
                end
            elseif M((n),1) > 200 && M((n),1) < 300
                if M((n),2)< (y(9)+rp)
                    if M((n),2)< (y(9))
                        M((n),5)=4;
                    else
                        M(n,5)=5;
                    end
                elseif M((n),2)< (y(7)+rp) && M((n),2)> (y(8)-rp)
                    if M((n),2)< (y(7)) && M((n),2)> (y(8))
                        M(n,5)=4;
                    elseif  M((n),2)< (y(7)+rp)
                        M(n,5)=5;
                    else
                        M(n,5)=6;
                    end
                elseif M((n),2)< (y(5)+rp) && M((n),2)> (y(6)-rp)
                    if M(ind(n),2)< (y(5)) && M((n),2)> (y(6))
                        M(n,5)=4;
                    elseif M((n),2)< (y(5)+rp)
                        M(n,5)=5;
                    else
                        M((n),5)=6;
                    end
                elseif M((n),2)> (y(4)-rp) && M((n),2)< (y(3)+rp)
                    if M((n),2)> (y(4)) && M((n),2)< (y(3)) %this is
not in the hb
                        M((n),5)=4;
                    elseif M((n),2)> (y(4)-rp)
                        M(n,5)=6;
                    else
                        M(n,5)=5;
                    end
                elseif M((n),2)> (y(2)-rp) && M((n),2)< (y(1)+rp)
                    if M((n),2)> (y(2)) && M((n),2)< (y(1))
                        M((n),5)=4;
                    elseif M((n),2)> (y(2)-rp)
                        M(n,5)=6;
                    else
                        M(n,5)=5;
                    end
                end

            end
             if M((n),3) > (top-rp) %this is so that no particles,
even if thay are in the HBs, can be higher than here
                    M((n),5)=1;
                end
        end

    end
```

```
      M((n+1),4)=streamnum;
      M(n+1,6)=count;

      %now create a higher order matrix where each streamline is in a
separate
      %dimension
      MM=zeros(400,6,streamnum);
      streamnum2=1;
      count=0;

      Endoflabling=clock

      %putting point in M in there appropriate part of MM
      for n=1:(length(M))
       MM(M(n,6),:,M(n,4))=M(n,:);
      end


      %% now rearrange M in order of increaseing x position for easier
point finding

      M=sortrows(M,1);

      save slant5020shorter.mat


      %% coding the initial matrix with wall proximity
      Init=zeros(streamnum,5);

      for i=1:streamnum
          Init(i,1)=init(i,1);
          Init(i,2)=init(i,2);
          Init(i,3)=init(i,3);
          Init(i,4)=1;
          n=i;

          if Init((n),2) < rp %first y wall
              Init(i,4)=0;
          elseif Init((n),2) > (200-rp) %2nd y wall
              Init(i,4)=0;
          elseif Init((n),3) < (rp) %channel bottom
              Init(i,4)=0;
          elseif Init((n),3) > (70-rp) %rectangular channel top
              %% the groove geometry (width) specific part

              y=[Init((n),1)+150;  Init((n),1)+100  ;Init((n),1)+50;
Init((n),1);  Init((n),1)-50;Init((n),1)-100;Init((n),1)-
150;Init((n),1)-200;Init((n),1)-250];
              if Init((n),1) < 50 % this set determines if it is in a
herringbone, if not then it is excluded after top-rp
                  if Init((n),2)> (y(4)-rp) && Init((n),2)< (y(3)+rp)
                     Init(i,4)=0;
                  elseif Init((n),2)> (y(2)-rp) && Init((n),2)<
(y(1)+rp)
                      Init(i,4)=0;
                  end
```

```
            elseif Init((n),1) > 50 && Init((n),1) < 100
                if Init((n),2)< (y(5)+rp)
                    Init(i,4)=0;
                elseif Init((n),2)> (y(4)-rp) && Init((n),2)<
(y(3)+rp)
                    Init(i,4)=0;
                elseif Init((n),2)> (y(2)-rp) && Init((n),2)<
(y(1)+rp)
                    Init(i,4)=0;
                end
            elseif Init((n),1) > 100 && Init((n),1) < 200
                if Init((n),2)< (y(7)+rp) && Init((n),2)> (y(8)-rp)
                    Init(i,4)=0;
                elseif Init((n),2)< (y(5)+rp) && Init((n),2)> (y(6)-
rp)
                   Init(i,4)=0;
                elseif Init((n),2)> (y(4)-rp) && Init((n),2)<
(y(3)+rp)
                    Init(i,4)=0;
                elseif Init((n),2)> (y(2)-rp) && Init((n),2)<
(y(1)+rp)
                    Init(i,4)=0;
                end
            elseif Init((n),1) > 200 && Init((n),1) < 300
                if Init((n),2)< (y(9)+rp)
                    Init(i,4)=0;
                elseif Init((n),2)< (y(7)+rp) && Init((n),2)> (y(8)-
rp)
                    Init(i,4)=0;
                elseif Init((n),2)< (y(5)+rp) && Init((n),2)> (y(6)-
rp)
                    Init(i,4)=0;
                elseif Init((n),2)> (y(4)-rp) && Init((n),2)<
(y(3)+rp)
                    Init(i,4)=0;
                elseif Init((n),2)> (y(2)-rp) && Init((n),2)<
(y(1)+rp)
                    Init(i,4)=0;
                end

            end
            if Init((n),3) > (top-rp) %this is so that no particles,
even if thay are in the HBs, can be higher than here
                Init(i,4)=0;
            end
        end
    end
    scatter(Init(:,2),Init(:,3),3,Init(:,4),'filled')

    % labeling streamlines exit grid with 0 if starting pt too close
to the wall
    endpts=zeros(streamnum,4);
    for i=1:streamnum
        if Init(i,4)==1
            yes=1;
        else
            yes=0;
```

```
            end
            A=length(nonzeros(MM(:,2,i)));
            if A>0
                xendpts= MM(A,1,i);
                yendpts= MM(A,2,i);
                zendpts= MM(A,3,i);
                ystarts= MM(1,2,i);
                if xendpts>198.5
                    endpts(i,1)=xendpts;
                    endpts(i,2)=yendpts;
                    endpts(i,3)=zendpts;
                    endpts(i,4)=yes;
                end
            end
        end

        scatter(endpts(:,2),endpts(:,3),3,endpts(:,4),'filled')

        %% finding and moving particles that hit the wall

        move=1; % number of microns it moves over, will need to make sure
streamline spacing is on this order!
        movecode=[0,move,0;0,-move,0;0,0,move;0,0,-move;0,1/2*move,0;0,-
1/2*move,0];

        for j=1:streamnum
            if max(MM(:,5,j))==0
                Init(j,5)=j;
            else
                if endpts(j,2)>0 && endpts(j,4)>0
                    endpts(j,4)=endpts(j,4)-1;
                end

                A=length(nonzeros(MM(:,2,j)));
                Q=[]; % is a temporary matrix that will hold a place for
the MM specified

                for k=1:A
                    Q=[Q;MM(k,:,j)];
                end
                pt=1;
                xpt=Q(pt,1);

                while xpt<198.5

                    if max(Q(:,5))==0
                        endptyz=[Q(A,2),Q(A,3)];
                        xpt=[Q(A,1)];
                    else
                        xpt=Q(pt,1);
                        while Q(pt,5)==0
                            pt=pt+1;
                        end

                        code=Q(pt,5);
                        newpt=[Q(pt,1),Q(pt,2),Q(pt,3)]+
movecode(code,:);
```

```
                        %find the closest poing on another streamline
                        mindist=50;
                        i=1; %check the dragonly code for fast way of
going throught the big matrix!!
                        while (M(i,1)-newpt(1)) < dist  && i < length(M)
                            if M(i,1)>newpt(1)
                                if abs((M(i,1)-newpt(1)))<(10)
                                    if abs((M(i,2)-newpt(2)))<(10)
                                        if abs((M(i,3)-newpt(3)))<(10)
                                            D=sqrt(((M(i,1)-
newpt(1)))^2+((M(i,2)-newpt(2)))^2+(((M(i,3)-newpt(3)))^2));
                                            if D<mindist
                                                if M(i,5)==0 &&
length(nonzeros(MM(:,2,(M(i,4)))))>20
                                                    mindist=D;
                                                    point=i; %stream
identifies the streamline that starts closest to this point
                                                end
                                            end
                                        end
                                    end
                                end
                            end
                            i=i+1;
                        end

                        stream=M(point,4);
                        stpt=M(point,6); %tells us where in MM to start
                        A=length(nonzeros(MM(:,2,stream))); %tells us end
of MM

                        Q=[];
                        %make a new matrix that goes for the point that
you moved to to the
                        %end

                        for m=stpt:A
                            Q=[Q;MM(m,:,stream)];
                        end
                        xpt=Q(1,1);
                        A=A-stpt+1;
                        pt=1;
                    end
                    streamid=stream;
                end
                Init(j,5)=streamid;
                endpts(streamid,4)=endpts(streamid,4)+1;
            end

        end

        %% mapp to the orignial grid
        endptgrid=zeros(streamnum,4);
        endptgridweight=zeros(streamnum,4);

        point1=0;
```

```
      point2=0;
      point3=0;
      point4=0;
      for j=1:streamnum
          mindist=[50;50;50;50];  %this is an arbitrarily large value
for the minimum distance between points
          for i=1:streamnum
              if abs((endpts(j,2)-Init(i,2)))<(10)
                  if abs((endpts(j,3)-Init(i,3)))<(10)
                      D=sqrt(((endpts(j,2)-Init(i,2))^2)+((endpts(j,3)-
Init(i,3))^2));
                      if D<mindist(1)
                          point4=point3;
                          mindist(4)=mindist(3);
                          point3=point2;
                          mindist(3)=mindist(2);
                          point2=point1;
                          mindist(2)=mindist(1);
                          mindist(1)=D;
                          point1=i;
                      elseif D<mindist(2)
                          point4=point3;
                          mindist(4)=mindist(3);
                          point3=point2;
                          mindist(3)=mindist(2);
                          mindist(2)=D;
                          point2=i;
                      elseif D<mindist(3)
                          point4=point3;
                          mindist(4)=mindist(3);
                          mindist(3)=D;
                          point3=i;
                      elseif D<mindist(4)
                          mindist(4)=D;
                          point4=i;
                      end
                  end
              end
          end

          endptgrid(j,1)=point1;
          endptgrid(j,2)=point2;
          endptgrid(j,3)=point3;
          endptgrid(j,4)=point4;

          weight=(1/mindist)/sum((1/mindist));
          endptgridweight(j,1)=weight(1);
          endptgridweight(j,2)=weight(2);
          endptgridweight(j,3)=weight(3);
          endptgridweight(j,4)=weight(4);

      end

      %%now we can interate!
      iterationspercycle=12;

      numcycles=12;
```

```
      totaliteration=iterationspercycle*numcycles;


      value=zeros(streamnum,totaliteration+1+2); %this matrix will have
the grid
      %point coordinates y, z in the first 2 columns, then the value
realting to
      %distribution probability for each point across each iteration

      value(:,1)=Init(:,2);
      value(:,2)=Init(:,3);

      %create starting point values all 1s on the entry side of the
channel
      for i=1:streamnum
          if Init(i,2)>rp && Init(i,2)< (100-rp) && Init(i,3)>rp &&
Init(i,3)< (70-rp)
              value(i,3)=1;
          end
      end


      Y=[];
      Z=[];
      Val=[];

      for i=1:streamnum
          if value(i,2)<70
              Y=[Y;value(i,1)];
              Z=[Z;value(i,2)];
              Val=[Val;value(i,3)];
          end
      end

      %create a concentration map of initial distribution
      parsize=73; %pixels
      parlen=floor(parsize/2);
      par=double(par);
      samplemap=zeros(70*10+2*parsize,200*10+2*parsize);

      for i=1:1:length(Y)
          pz=Z(i)*10+parsize;
          py=Y(i)*10+parsize;
          samplemap(pz-parlen:1:pz+parlen, py-
parlen:1:py+parlen)=samplemap(pz-parlen:1:pz+parlen, py-
parlen:1:py+parlen)+par*Val(i);
      end
      map=samplemap(end-parsize:-1:parsize+1,parsize+1:1:end-parsize);

      mapp= uint8(map);
      mapp= imadjust(mapp,stretchlim(map, [0,1]),[]); %stretchlim(map)
      high=max(mapp);
      high=max(high);

      imshow(mapp,[0,high],'InitialMagnification',20)
```

```
      name2=strcat('slant5020_',int2str(bead),'beaddensitymap_cycles_',
int2str(0),'.jpg');
      saveas(gcf, name2,'jpg')

      %iterated by moving intial values, to endpoint grid, then
remapping and
      %repeat
      for i=1:totaliteration
          n=i+3;
          for j=1:streamnum
              endstream=Init(j,5);

value(endptgrid(endstream,1),n)=value(endptgrid(endstream,1),n)+endptgr
idweight(endstream,1)*value(j,n-1);

value(endptgrid(endstream,2),n)=value(endptgrid(endstream,2),n)+endptgr
idweight(endstream,2)*value(j,n-1);

value(endptgrid(endstream,3),n)=value(endptgrid(endstream,3),n)+endptgr
idweight(endstream,3)*value(j,n-1);

value(endptgrid(endstream,4),n)=value(endptgrid(endstream,4),n)+endptgr
idweight(endstream,4)*value(j,n-1);
          end
          if rem(i,6)==0
              Y=[];
              Z=[];
              Val=[];
              for k=1:streamnum
                  if value(k,2)<70
                      Y=[Y;value(k,1)];
                      Z=[Z;value(k,2)];
                      Val=[Val;value(k,3+i)];
                  end
              end

              parsize=73; %pixels
              parlen=floor(parsize/2);
              par=double(par);
              samplemap=zeros(70*10+2*parsize,200*10+2*parsize);

              for k=1:1:length(Y)
                  pz=Z(k)*10+parsize;
                  py=Y(k)*10+parsize;
                  samplemap(pz-parlen:1:pz+parlen, py-
parlen:1:py+parlen)=samplemap(pz-parlen:1:pz+parlen, py-
parlen:1:py+parlen)+par*Val(k);
              end
              map=samplemap(end-parsize:-1:parsize+1,parsize+1:1:end-
parsize);

              mapp= uint8(map);
              mapp= imadjust(mapp,stretchlim(map, [0,1]),[]);
%stretchlim(map)
              high=max(mapp);
              high=max(high);
```

```
                imshow(mapp,[0,high],'InitialMagnification',20)

name2=strcat('slant5020_',int2str(bead),'beaddensitymap_cycles_',int2st
r(i/12),'.jpg');

                saveas(gcf, name2,'jpg')
            end
        end

        save slant5020.mat

        name=strcat('slant5020_',int2str(bead),'bead_densitymap.xls');

        xlswrite(name,value)
```

REFERENCES

1. Janes, K.A., et al., *A systems model of signaling identifies a molecular basis set for cytokine-induced apoptosis.* Science, 2005. **310**(5754): p. 1646-53.

2. Reya, T. and H. Clevers, *Wnt signalling in stem cells and cancer.* Nature, 2005. **434**(7035): p. 843-50.

3. Sander, C., *Genomic medicine and the future of health care.* Science, 2000. **287**(5460): p. 1977-8.

4. Gibbs, J.B., *Mechanism-based target identification and drug discovery in cancer research.* Science, 2000. **287**(5460): p. 1969-73.

5. Yee, C., et al., *Melanocyte Destruction after Antigen-specific Immunotherapy of Melanoma: Direct Evidence of T Cell-mediated Vitiligo.* The Journal of Experimental Medicine, 2000. **192**(11): p. 1637-1644.

6. Dudley, M.E., et al., *Cancer regression and autoimmunity in patients after clonal repopulation with antitumor lymphocytes.* Science, 2002. **298**(5594): p. 850-4.

7. June, C.H., *Adoptive T cell therapy for cancer in the clinic.* J Clin Invest, 2007. **117**(6): p. 1466-76.

8. Morgan, R.A., et al., *Cancer Regression in Patients After Transfer of Genetically Engineered Lymphocytes.* Science, 2006. **314**(5796): p. 126-129.

9. Barber, L.D., et al., *HLA class I mono-specific APCs and target cells: a method to standardise in vitro CD8+ T cell expansion and functional assays.* J Immunol Methods, 2006. **314**(1-2): p. 147-52.

10. Janes, K.A., et al., *A high-throughput quantitative multiplex kinase assay for monitoring information flow in signaling networks: application to sepsis-apoptosis.* Mol Cell Proteomics, 2003. **2**(7): p. 463-73.

11. Kemp, M.L., et al., *Quantitative network signal combinations downstream of TCR activation can predict IL-2 production response.* Journal of Immunology, 2007. **178**(8): p. 4984-4992.

12. Kohrt, H.E., et al., *Rapid assessment of recognition efficiency and functional capacity of antigen-specific T-cell responses.* J Immunother (1997), 2005. **28**(4): p. 297-305.

13. Sachs, K., et al., *Causal Protein-Signaling Networks Derived from Multiparameter Single-Cell Data.* Science, 2005. **308**(5721): p. 523-529.

14. Pawelec, G., et al., *Human immunosenescence: is it infectious?* Immunological Reviews, 2005. **205**: p. 257-268.

15. Kemp, M.L., et al., *Quantitative Network Signal Combinations Downstream of TCR Activation Can Predict IL-2 Production Response.* J Immunol, 2007. **178**(8): p. 4984-92.

16. Kholodenko, B.N., et al., *Quantification of short term signaling by the epidermal growth factor receptor.* Journal of Biological Chemistry, 1999. **274**(42): p. 30169-30181.

17. Germain, R.N. and I. Stefanova, *The dynamics of T cell receptor signaling: complex orchestration and the key roles of tempo and cooperation.* Annu Rev Immunol, 1999. **17**: p. 467-522.

18. Kim, J.E. and F.M. White, *Quantitative analysis of phosphotyrosine signaling networks triggered by CD3 and CD28 costimulation in Jurkat cells.* J Immunol, 2006. **176**(5): p. 2833-43.

19. Gaudet, S., et al., *A Compendium of Signals and Responses Triggered by Prodeath and Prosurvival Cytokines.* Mol Cell Proteomics, 2005. **4**(10): p. 1569-1590.

20. Schoeberl, B., et al., *Computational modeling of the dynamics of the MAP kinase cascade activated by surface and internalized EGF receptors.* Nat Biotechnol, 2002. **20**(4): p. 370-5.

21. El-Ali, J., P.K. Sorger, and K.F. Jensen, *Cells on chips.* Nature, 2006. **442**(7101): p. 403-411.

22. Whitesides, G.M., *The origins and the future of microfluidics.* Nature, 2006. **442**(7101): p. 368-373.

23. Groisman, A., et al., *A microfluidic chemostat for experiments with bacterial and yeast cells.* Nature Methods, 2005. **2**(9): p. 685-689.

24. Paliwal, S., et al., *MAPK-mediated bimodal gene expression and adaptive gradient sensing in yeast.* Nature, 2007. **446**: p. 46-51.

25. King, K.R., et al., *Microfluidic flow-encoded switching for parallel control of dynamic cellular microenvironments.* Lab on a Chip, 2008. **8**(1): p. 107-116.

26. El-Ali, J., et al., *Cell stimulus and lysis in a microfluidic device with segmented gas-liquid flow.* Analytical Chemistry, 2005. **77**(11): p. 3629-3636.

27. Lu, H., M.A. Schmidt, and K.F. Jensen, *A microfluidic electroporation device for cell lysis.* Lab On A Chip, 2005. **5**(1): p. 23-29.

28. McClain, M.A., et al., *Microfluidic devices for the high-throughput chemical analysis of cells.* Anal. Chem, 2003. **75**(21): p. 5646–5655.

29. Sims, C.E. and N.L. Allbritton, *Analysis of single mammalian cells on-chip.* Lab on a Chip, 2007. **7**(4): p. 423-440.

30. Lee, P.J., et al., *Nanoliter scale microbioreactor array for quantitative cell biology.* Biotechnol. Bioeng, 2006. **94**(1): p. 5–14.

31. Carlo, D.D., et al., *On-chip cell lysis by local hydroxide generation.* Lab on a Chip, 2005. **5**(2): p. 171-178.

32. Herr, A.E., et al., *Microfluidic immunoassays as rapid saliva-based clinical diagnostics.* Proceedings of the National Academy of Sciences, 2007. **104**(13): p. 5268.

33. Stone, H.A., A.D. Stroock, and A. Ajdari, *Engineering Flows In Small Devices.* Annu. Revi. Fluid Mech., 2004. **36**(1): p. 381-411.

34. Hessel, V., H. Löwe, and F. Schönfeld, *Micromixers—a review on passive and active mixing principles* Chem. Eng. Sci., 2005. **60**(8-9): p. 2479-2501.

35. El-Ali, J., et al., *Cell stimulus and lysis in a microfluidic device with segmented gas-liquid flow.* Anal. Chem., 2005. **77**(11): p. 3629-36.

36. Hirsch, A.M., et al., *Parallel multi-time point cell stimulation and lysis on-chip for studying early signaling events in T cell activation.* Lab on a Chip, 2009. **9**(4): p. 536 - 544.

37. Stroock, A.D., et al., *Chaotic mixer for microchannels.* Science, 2002. **295**(5555): p. 647-651.

38. Toner, M. and D. Irimia, *Blood-On-A-Chip.* Annu. Rev. Biomed. Eng., 2005. **7**(1): p. 77-103.

39. Giddings, J.C., *Field-Flow Fractionation: Analysis of Macromolecular, Colloidal, and Particulate Materials.* Science, 1993. **260**(5113): p. 1456-1465.

40. Nolan, J.P. and L.A. Sklar, *The emergence of flow cytometry for sensitive, real-time measurements of molecular interactions.* Nat Biotech, 1998. **16**(1): p. 633-638.

41. Toner, M. and D. Irimia, *BLOOD-ON-A-CHIP.* Annual Review of Biomedical Engineering, 2005. **7**(1): p. 77-103.

42. Mott, D.R., et al., *Toolbox for the design of optimized microfluidic components.* Lab on a Chip, 2006. **6**(4): p. 540-549.

43. Di Carlo, D., et al., *Particle Segregation and Dynamics in Confined Flows.* Physical Review Letters, 2009. **102**(9): p. 094503.

44. Di Carlo, D., et al., *Continuous inertial focusing, ordering, and separation of particles in microchannels.* Proceedings of the National Academy of Sciences, 2007. **104**(48): p. 18892-18897.

45. Park, J.-S., S.-H. Song, and H.-I. Jung, *Continuous focusing of microparticles using inertial lift force and vorticity via multi-orifice microfluidic channels.* Lab on a Chip, 2009. **9**(7): p. 939-948.

46. Abkarian, M., et al., *Cellular-scale hydrodynamics.* Biomed Mater, 2008. **3**(3): p. 034011.

47. Gao, C. and J.F. Gilchrist, *Shear-induced particle migration in one-, two-, and three-dimensional flows.* Physical Review E, 2008. **77**(2): p. 025301.

48. Hsu, C.-H., et al., *Microvortex for focusing, guiding and sorting of particles.* Lab on a Chip, 2008. **8**(12): p. 2128-2134.

49. Segre, G. and A. Silberberg, *Radial Particle Displacements in Poiseuille Flow of Suspensions.* Nature, 1961. **189**(4760): p. 209-210.

50. Semwogerere, D. and E.R. Weeks, *Shear-induced particle migration in binary colloidal suspensions.* Phys. Fluids, 2008. **20**(4): p. 043306.

51. Murata, S. and M. Kawamura, *Particle depth measurement based on depth-from-defocus.* Opt. Laser Technol., 1999. **31**(1): p. 95-102.

52. Choi, S. and J.K. Park, *Mirror-embedded microchannel for three-dimensional measurement of particle position.* Appl. Phys. Lett., 2008. **93**(19): p. 191909.

53. Lin, D.J., et al., *Three-dimensional particle imaging by defocusing method with an annular aperture.* Opt. Lett., 2008. **33**(9): p. 905-907.

54. Luo, R., et al., *Tracking sub-micron fluorescent particles in three dimensions with a microscope objective under non-design optical conditions.* Meas. Sci. Tech., 2006. **17**: p. 1358-1366.

55. Park, J.S., C.K. Choi, and K.D. Kihm, *Temperature measurement for a nanoparticle suspension by detecting the Brownian motion using optical serial sectioning microscopy (OSSM).* Meas. Sci. Technol., 2005. **16**: p. 1418-1429.

56. Pereira, F., et al., *Microscale 3D flow mapping with μDDPIV.* Exp. Fluids, 2007. **42**(4): p. 589-599.

57. Wu, M.M., J.W. Roberts, and M. Buckley, *Three-dimensional fluorescent particle tracking at micron-scale using a single camera.* Exp. Fluids, 2005. **38**(4): p. 461-465.

58. Yoon, S.Y. and K.C. Kim, *3D particle position and 3D velocity field measurement in a microvolume via the defocusing concept.* Meas. Sci. Technol., 2006. **17**(11): p. 2897-2905.

59. Park, J.S. and K.D. Kihm, *Three-dimensional micro-PTV using deconvolution microscopy* Exp. Fluids, 2006. **40**(3): p. 491-499.

60. Lindken, R., et al., *Micro-Particle Image Velocimetry ([small micro]PIV): Recent developments, applications, and guidelines.* Lab on a Chip, 2009. **9**(17): p. 2551-2567.

61. Born, M. and E. Wolf, *Principles of Optics*. 1965, New York: Pergamon.

62. Huang, L.R., et al., *Continuous Particle Separation Through Deterministic Lateral Displacement.* Science, 2004. **304**(5673): p. 987-990.

63. Yamada, M. and M. Seki, *Hydrodynamic filtration for on-chip particle concentration and classification utilizing microfluidics.* Lab on a Chip, 2005. **5**(11): p. 1233-1239.

64. Salieb-Beugelaar, G.B., et al., *Latest Developments in Microfluidic Cell Biology and Analysis Systems.* Analytical Chemistry, 2010. **82**(12): p. 4848-4864.

65. Sudarsan, A.P. and V.M. Ugaz, *Multivortex micromixing.* Proceedings of the National Academy of Sciences, 2006. **103**(19): p. 7228-7233.

66. Stroock, A.D., et al., *Chaotic mixer for microchannels.* Science, 2002. **295**(5555): p. 647-651.

67. Howell, P.B., et al., *A microfluidic mixer with grooves placed on the top and bottom of the channel.* Lab on a Chip, 2005. **5**(5): p. 524-530.

68. Yang, J.T., K.J. Huang, and Y.C. Lin, *Geometric effects on fluid mixing in passive grooved micromixers.* Lab on a Chip, 2005. **5**(10): p. 1140-1147.

69. Xia, Y.N. and G.M. Whitesides, *Soft lithography.* Annual Review of Materials Science, 1998. **28**: p. 153-184.

70. Migliori, M., et al., *Viscosity of multicomponent solutions of simple and complex sugars in water.* Journal of Chemical and Engineering Data, 2007. **52**(4): p. 1347-1353.

71. Deen, W.M., *Analysis of Transport Phenomena* 1998, New York, New York: Oxford University Press, Inc.

72. Lam, L.T., et al., *Small Molecule Inhibitors of I{kappa}B Kinase Are Selectively Toxic for Subgroups of Diffuse Large B-Cell Lymphoma Defined by Gene Expression Profiling.* Clinical Cancer Research, 2005. **11**(1): p. 28-40.

73. Wu, S.P., et al., *Wall shear rates differ between the normal carotid, femoral, and brachial arteries: An in vivo MRI study.* Journal of Magnetic Resonance Imaging, 2004. **19**(2): p. 188-193.

74. Khan, I.H., et al., *Multiplex analysis of intracellular signaling pathways in lymphoid cells by microbead suspension arrays.* Mol Cell Proteomics, 2006. **5**(4): p. 758-68.

75. Besseling, R., et al., *Quantitative imaging of colloidal flows.* Advances in Colloid and Interface Science, 2009. **146**(1-2): p. 1-17.

76. Gao, C., B. Xu, and J.F. Gilchrist, *Mixing and segregation of microspheres in microchannel flows of mono- and bidispersed suspensions.* Physical Review E, 2009. **79**(3): p. 036311.

77. Davies, D., *Cell Sorting by Flow Cytometry*, in *Flow Cytometry: Principles and Application*, M.G. Macey, Editor. 2007, Humana Press Inc: Totowa, NJ. p. 257-276.

78. Petersson, F., et al., *Free Flow Acoustophoresis:â€‰ Microfluidic-Based Mode of Particle and Cell Separation.* Analytical Chemistry, 2007. **79**(14): p. 5117-5123.

79. Hu, X., et al., *Marker-specific sorting of rare cells using dielectrophoresis.* Proceedings of the National Academy of Sciences of the United States of America, 2005. **102**(44): p. 15757-15761.

80. Taff, B.M. and J. Voldman, *A Scalable Addressable Positive-Dielectrophoretic Cell-Sorting Array.* Analytical Chemistry, 2005. **77**(24): p. 7976-7983.

81. Liu, Y.-J., et al., *A micropillar-integrated smart microfluidic device for specific capture and sorting of cells.* ELECTROPHORESIS, 2007. **28**(24): p. 4713-4722.

82. Kang, J.H., et al., *Isomagnetophoresis to Discriminate Subtle Difference in Magnetic Susceptibility.* Journal of the American Chemical Society, 2007. **130**(2): p. 396-397.

83. Wang, M.M., et al., *Microfluidic sorting of mammalian cells by optical force switching.* Nat Biotech, 2005. **23**(1): p. 83-87.

84. MacDonald, M.P., G.C. Spalding, and K. Dholakia, *Microfluidic sorting in an optical lattice.* Nature, 2003. **426**(6965): p. 421-424.

85. Choi, S., et al., *Hydrophoretic Sorting of Micrometer and Submicrometer Particles Using Anisotropic Microfluidic Obstacles.* Analytical Chemistry, 2008. **81**(1): p. 50-55.

86. Choi, S., et al., *Continuous blood cell separation by hydrophoretic filtration.* Lab on a Chip, 2007. **7**(11): p. 1532-1538.

87. Mach, A.J. and D. Di Carlo, *Continuous scalable blood filtration device using inertial microfluidics.* Biotechnology and Bioengineering. **107**(2): p. 302-311.

88. Hur, S.C., A.J. Mach, and D. Di Carlo, - *High-throughput size-based rare cell enrichment using microscale vortices.* **- 5**(- 2).

89. Howell Jr, P.B., et al., *Two simple and rugged designs for creating microfluidic sheath flow.* Lab on a Chip, 2008. **8**(7): p. 1097-1103.

90. Golden, J.P., et al., *Multi-wavelength microflow cytometer using groove-generated sheath flow.* Lab on a Chip, 2009. **9**(13): p. 1942-1950.

91. Camesasca, M. and et al., *Entropic characterization of mixing in microchannels.* Journal of Micromechanics and Microengineering, 2005. **15**(11): p. 2038.

92. Camesasca, M., M. Kaufman, and I. Manas-Zloczower, *Quantifying Fluid Mixing with the Shannon Entropy.* Macromolecular Theory and Simulations, 2006. **15**(8): p. 595-607.

93. Agbudeloye, A. and I.E. Barton, *A consistent Eulerian and Lagrangian approach for dilute particulate flows*, in *Advances in Fluid Mechanics*, M. Rahaman, Editor. 2000, Wessex Institute of Technology Press: Dalhousie University, Canada.

94. Benczik, I.J., et al., *Advection of finite-size particles in open flows.* Physical Review E, 2003. **67**(3): p. 036303.

95. Greengard, L. and V. Rokhlin, *A fast algorithm for particle simulations.* Journal of Computational Physics, 1987. **73**(2): p. 325-348.

96. Nott, P.R. and J.F. Brady, *Pressure-driven flow of suspensions: simulation and theory.* Journal of Fluid Mechanics, 1994. **275**: p. 157-199.

97. Maxey, M.R. and J.J. Riley, *Equation of motion for a small rigid sphere in a nonuniform flow.* Physics of Fluids, 1983. **26**(4): p. 883-889.

98. Nguyen, N.Q. and A.J.C. Ladd, *Lubrication corrections for lattice-Boltzmann simulations of particle suspensions.* Physical Review E, 2002. **66**(4): p. 046708.

99. Wagner, G.J., S. Ghosal, and W.K. Liu, *Particulate flow simulations using lubrication theory solution enrichment.* International Journal for Numerical Methods in Engineering, 2003. **56**(9): p. 1261-1289.

100. Rivet, C.A., et al., *Predicting Cytotoxic T-cell Age from Multivariate Analysis of Static and Dynamic Biomarkers.* Molecular & Cellular Proteomics. **10**(3).